Porous titania/carbon hybrid microspheres templated by *in situ* formed polystyrene colloids

Ting Cheng [a,b], Guoqiang Zhang [c], Yonggao Xia [a], Zaicheng Sun [c], Zhaohui Yang [d], Rui Liu [e], Ying Xiao [a], Xiaoyan Wang [a,f], Meimei Wang [a,b], Jianzhen Ban [a,g], Liangtao Yang [a,g], Qing Ji [a], Bao Qiu [a], Guoxin Chen [a], Huifeng Chen [a], Yichao Lin [a], Xiaoying Pei [a], Qiang Wu [d], Jian-Qiang Meng [f], Zhaoping Liu [a], Liang Chen [a], Tonghu Xiao [b], Ling-Dong Sun [e], Chun-Hua Yan [e], Hans Jürgen Butt [h], Ya-Jun Cheng [a,*]

[a] *Ningbo Institute of Materials Technology and Engineering, Chinese Academy of Sciences, 1219 Zhongguan West Rd, Zhenhai District, Ningbo, Zhejiang Province 315201, PR China*
[b] *Faculty of Materials Science and Chemical Engineering, Ningbo University, Ningbo, Zhejiang Province 315211, PR China*
[c] *Changchun Institute of Optics, Fine Mechanics and Physics, Chinese Academy of Sciences, State Key Laboratory of Luminescence & Applications, 3888 East Nanhu Rd, Changchun 130033, PR China*
[d] *Soochow University, Center for Soft Condensed Matter Physics & Interdisciplinary Research, Suzhou 215006, PR China*
[e] *Beijing National Laboratory for Molecular Sciences, State Key Laboratory of Rare Earth Materials Chemistry and Applications & PKU-HKU Joint Lab on Rare Earth Materials and Bioinorganic Chemistry, College of Chemistry and Molecular Engineering, Peking University, Beijing 100871, PR China*
[f] *State Key Laboratory of Separation Membranes and Membrane Processes, Tianjin Polytechnic University, Tianjin 300387, PR China*
[g] *Nano Science and Technology Institute, University of Science and Technology of China, Suzhou 215123, PR China*
[h] *Max-Planck Institute for Polymer Research, Ackermannweg 10, D-55128 Mainz, Germany*

GRAPHICAL ABSTRACT

Hierarchical porous TiO_2/carbon hybrid microspheres have been synthesized, using *in situ* formed polystyrene colloids as templating agent and carbon source under solvothermal reaction.

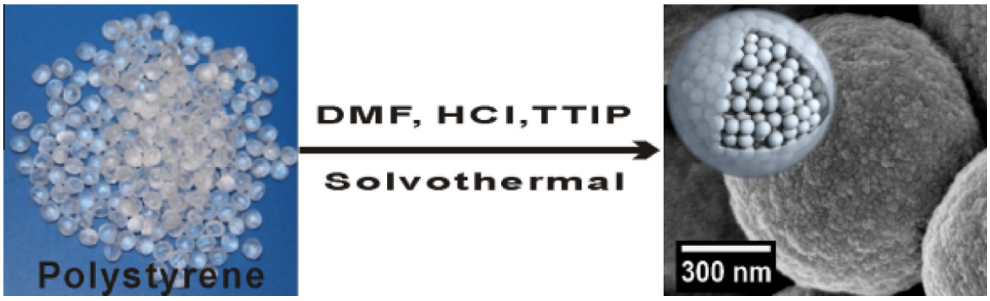

ARTICLE INFO

Keywords:
Titania/carbon hybrid
Microsphere

ABSTRACT

A new strategy to synthesize hierarchical, porous titania/carbon (TiO_2/C) hybrid microspheres via solvothermal reaction in N,N′-dimethyl formamide (DMF) has been developed. *In situ* formed polystyrene (PS) colloids have been used as templating agent and carbon source, through which TiO_2/PS microspheres with a diameter of *ca.* 1 μm are built by packed TiO_2 nanoparticles of tens of nanometers. The TiO_2/PS microspheres are converted to TiO_2/C microspheres with different amounts of carbon under controlled calcination condition. The mechanism investigation unveils that the introduction of concentrated HCl creates surface tension between PS and DMF, leading to the formation of PS colloids in solution. The solvothermal treatment further promotes the formation of PS colloids and integration of the titania

* Corresponding author.
E-mail address: chengyj@nimte.ac.cn (Y.-J. Cheng).

nanoparticles within the PS colloids. The morphology, crystallinity, nature and content of carbon, UV–Vis absorption, carbon doping, pore size distribution, pore volume, and BET surface area of the TiO_2 microspheres with different amounts of carbon have been measured. The applications of the TiO_2/C hybrid microspheres as photo catalyst for water splitting and lithium-ion battery anode have been demonstrated. Superior photo catalytic activity for hydrogen conversion under both full spectrum and visible light illumination compared to commercial P25 has been observed for the TiO_2/C microspheres with 2 wt% of carbon. Besides, the TiO_2/C microspheres with 8 wt% of carbon as lithium-ion battery anode showed a much higher capacity than the bare TiO_2 microsphere anode. The origin for the enhanced performance as photo catalyst and lithium-ion battery anode is discussed.

1. Introduction

TiO_2 has broad applications in coating, dye-sensitized solar cells, photocatalysis, lithium ion batteries, and sensors due to its abundance, low toxicity, and unique electrochemical properties [1–7]. Crystallinity, morphology and surface coating of TiO_2 play important roles in the performance of the devices [8–14]. Recently hierarchical architectures composed of both nano-sized primary structures and micrometer scale secondary aggregates attracted considerable attention. While the nanostructures offer high specific surface area, short charge carrier transportation routes and high electrochemical reactivity; the micrometer-scale aggregates provide high tap density and good bulk structure stability [15–17]. In addition to a control of the morphology, compositing TiO_2 with carbon is an effective strategy to modify the absorption wavelength, optimize fundamental electrochemical process, and improve intrinsic electron conductivity of TiO_2 [18–24]. Combining these two strategies is essential to achieve good overall performance in photocatalysis and lithium-ion batteries.

Numerous strategies have been developed to synthesize hierarchical TiO_2 microspheres including hard/soft template, emulsification, and template free reaction [15,25–40]. Solid polymer beads such as polystyrene (PS) or poly (methyl methacrylate) (PMMA) have been extensively used as templates to synthesize porous TiO_2 [15,25,30,32,40–42]. However, severe drawbacks remain with this strategy. First, synthesis of well-defined polymer beads is required, which significantly limits the feasibility of this strategy. Second, a two-phase reaction feature dominates when PS and PMMA solids are used as scaffolds to soak the precursor of TiO_2 [43]. It makes it very difficult to control the interaction between the liquid TiO_2 sol–gel precursor solution and solid plastic matrix. Regarding the emulsification method, the synthesized TiO_2 microspheres are mainly decorated with small molecule surfactant, which can hardly be converted to surface carbon coating [15,28,29,31,37]. Besides small surfactants, amphiphilic block copolymers or hydrophilic polymers are also used as templating agents [26,44–49]. However, due to the aliphatic nature of the polymer chains, the content of carbon formed after calcination is rather limited, leading to insufficient carbon coating. Furthermore, some of the amphiphilic block copolymers are quite expensive and therefore inconvenient to access. The template free reaction is also reported to generate TiO_2 microspheres under certain conditions, but template free implies that the synthesized TiO_2 microspheres lack carbon coating [15,35,50].

Here, we report a new approach to synthesize hierarchical, porous TiO_2 microspheres with controlled carbon content. *In situ* formed PS colloids are used as both, templating agent and carbon source. As shown in Scheme 1, PS is first dissolved in N,N′-dimethyl formamide (DMF), followed by addition of concentrated HCl. PS colloids are formed in solution due to the interfacial tension introduced by the concentrated HCl. By using titanium tetraisopropoxide (TTIP) as precursor and further solvothermal treatment, TiO_2/PS hybrid microspheres are synthesized. Via calcination in argon, TiO_2/C hybrid microspheres are synthesized. Furthermore, by treating the TiO_2/C microspheres with consecutive heat in air at moderate temperature (300 °C) for different time range (0.5–1.5 h), the contents of carbon within the TiO_2 microspheres are systematically tuned.

By comparing our strategy with the previously reported strategies based on the PS templates, one significant difference remains. With our strategy, it is the *in situ* formed PS colloids rather than the simple solid PS matrix acting as the template. This particular feature circumvents the typical two-phase reaction process associated with the solid PS templates. It offers delicate control over morphology and significant expansion of the templating capability of PS. Besides, with our strategy no preliminary synthesis of well-defined polymer beads is required. Despite of the above advantages, to our best knowledge, the dissolved PS has been rarely used as templating agent for the synthesis of nanostructured metal oxides compared to the intensively utilized hydrophilic polymer templates. The reason may lie in the fact that it is intuitively assumed that the hydrophobic chemically inert PS does not possess strong interactions with hydrophilic reactive metal oxide precursors. The dissolved PS is regarded as unlikely to exercise as a good templating agent [25,51].

2. Experiment

All chemicals and materials addressed in this work were used as received without further purification. DMF of analytical grade and concentrated HCl (37%) were received from Sinopharm Group Co., Ltd. Titanium tetraisopropoxide (TTIP, 97%) was purchased from Alfa Aesar. Si (100) wafers (Shanghai JunHe Electronic Materials Co., Ltd.) were used as substrates for spin coating the PS solutions after solvothermal treatment. Polystyrene from Sigma Aldrich was used (average molecular weight M_w of 192,000). TiO_2 nanoparticles (P25) were purchased from Evonik Industries AG. Amphiphilic block copolymer of polystyrene-*block*-poly (ethylene oxide) (PS-*b*-PEO) was synthesized in house via a sequential anionic polymerization. The number average molecular weight was 6.2 kg/mol for PS and 18.6 kg/mol for PEO with a polydispersity of 1.04.

Typical sample preparation procedure was as following. 0–1.6 g PS was dissolved in 10 g of DMF under continuous stirring. Thereafter, concentrated HCl (from 0 g to 0.8 g) and TTIP (from 0 g to 0.8 g) were added and the solution was stirred further for around 10 min. In the case PS-*b*-PEO was used as a co-templating agent, from 0 g to 1 g of PS-*b*-PEO was added. The solution was transferred to a Teflon-lined stainless steel autoclave and heated at 110 °C for 4 h with a ramp rate of 5 K/min starting from room temperature. After the solvothermal treatment was finished, the autoclave was cooled down to room temperature in muffle furnace. The white precipitates formed were centrifuged and washed with ethanol for three times. Then the precipitates were dried at 80 °C in vacuum for 24 h.

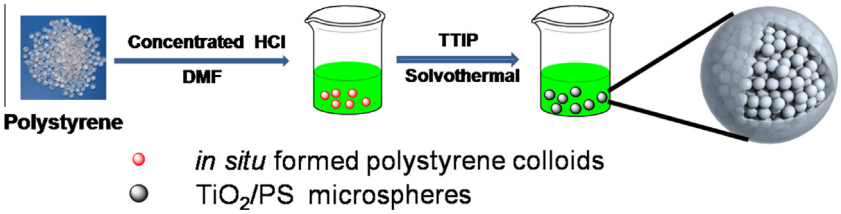

Scheme 1. Solvothermal synthesis of hierarchical TiO_2 microspheres templated by *in situ* formed polystyrene colloids.

The calcination in air was conducted in muffle furnace at 500 °C for 3 h with a ramp rate of 5 K/min from room temperature, followed by natural cooling to room temperature in the furnace. Calcination in argon was carried out in a tube furnace using the same protocol. To partially remove carbon coating, the TiO_2/carbon hybrids were further heated in air in muffle furnace at 300 °C for 0.5 h and 1.5 h respectively.

Field emission scanning electron microscopy (FESEM) images were obtained in a Hitachi S4800 scanning electron microscope (Tokyo, Japan) at an accelerating voltage of 4 kV. The sample powder was put on a conductive tape and sputtered with gold before imaging.

Transmission electron microscopy (TEM) experiment of the one-step calcination samples were conducted by putting a drop of aqueous suspension containing TiO_2 on a carbon-supported copper grid and measured with an FEI Tecnai F20 TEM (Oregon, USA) with a 200 kV field emission gun. The as-prepared and tandem calcination samples were further examined by a TEM (2100F, JEOL, Japan) operated at 200 kV using the identical sample preparation protocol.

The crystallographic phases of the powders were characterized by X-ray diffraction (XRD) (Bruker AXS D8 Advance, λ = 1.541 Å, 2.2 kW) with 2θ ranged from 5° to 90°. The content of the carbon coated on the TiO_2 surface was determined by thermo gravimetric analyzer (TGA, Mettler Toledo, Switzerland) with the temperature range between 50 °C and 800 °C at a ramp rate of 20 K/min. X-ray photoelectron spectroscopy (XPS) measurement was carried out with an ESCALAB 250Xi spectrometer, using focused mono chromatized Al Kα radiation ($h\nu$ = 1486.6 eV) at room temperature. Nitrogen adsorption–desorption isotherms were measured with an ASAP 2020 M apparatus at 77.3 K. In a general procedure, the dry sample (*ca.* 200 mg) was loaded into the glass analysis tube. Then the glass tube was fixed to the degas port. The heating and evacuation procedure includes two stages. The temperature was firstly increased to 90 °C with a ramp rate of 10 K/min and then held for 30 min. Thereafter, the temperature was increased to 200 °C and held for 8 h until the outgas rate was less than 5 μm Hg. The sample was then backfilled with N_2 before transferred to the analysis port. N_2 adsorption–desorption isotherm was measured at 77.3 K and the range of relative pressures was set between 0 and 1.0. The BET surface area was calculated over the range of relative pressures between 0.05 and 0.20. Raman spectroscopy was recorded with Renishaw (inVia-reflex).

The UV–Vis Measurements were carried out using Lambda 950. The Sample preparation was as following. $BaSO_4$ was used as substrate by putting certain amount of $BaSO_4$ at the bottom of sample vial and pressing it into plates. Thereafter, around 50 mg of the samples were put on the surface of $BaSO_4$ and pressed into plate as well.

The photoluminescence experiment was carried out on Perkin Elmer LS55 Fluorescence Spectrometer using a 350 nm laser as the excitation source and an emission range of between 400 nm and 750 nm. Each data point is averaged based on five scans. Identical amount of samples were used to measure the intensity of the photoluminescence.

The tap densities of the TiO_2 powder and TiO_2/C hybrids were measured according to GB/T 5162-2006. Similar amount of TiO_2 and TiO_2/C powders were put in two graduates of 1 ml separately. The graduates were vibrated manually for more than 3000 times until no volume change was observed by naked eyes. The final volume was measured and the corresponding densities of the powders were calculated.

Small-angle X-ray scattering (SAXS) measurements were performed on a Ganesha 300XL SAXS-WAXS system (SAXS LAB ApS, Copenhagen/Denmark). The X-ray radiation was produced at 50 kV/0.6 mA from a Cu anode with a wavelength λ = 0.154 nm. The sample-to-detector distance was 406 mm. The sample powder was put into a glass capillary which functioned as a holder and allowed X-ray transmission (SAXS) experiments. The 2D SAXS data were radially averaged and presented in logarithmic scattering intensity versus the magnitude of the scattering vector, $q = 4\pi * \sin(\Theta)/\lambda$, where 2Θ is the scattering angle. The SAXS data were fitted using SASfit software.

Photo catalytic activity measurements were carried out according to the following procedure. 50 mg of TiO_2 or TiO_2/C powders were placed under dark condition and dispersed into an aqueous methanol solution (120 ml, 25 vol.%) in a closed gas circulation system (Perfect Light Company Labsolar-III (AG)). The UV–Vis light irradiations were obtained from a 300 W Xe lamp (Perfect Light Company Solaredge 700) without and with a UVCUT-420 nm filter (CE Aulight Inc.). The evolved gases were detected *in situ* by using an online gas chromatograph (GC-2014C, Shimadzu) equipped with a thermal conductivity detector (TCD).

Electrochemical performance of the TiO_2/C powders as lithium ion battery anodes was measured as following. 2032-type coin cells were employed to evaluate the electrochemical performance of the TiO_2 and TiO_2/C anodes. A slurry mixture was prepared by dispersing active material, Super P and poly (vinylidene fluoride) (PVDF) (mass ratio: 8:1:1) in N-methyl Pyrrolidone. The electrodes were prepared by spreading the slurry mixture on a piece of copper foil, followed by drying at 80 °C overnight. The copper foil was pressed, cut into appropriate dimension, and dried in over at 80 °C further for 4 h. Lithium foil was used as the counter electrode. Electrolyte from Shanshan Tech Co., Ltd was used; where 1.0 M $LiPF_6$ was dissolved in a mixture of ethylene carbonate (EC) and diethyl carbonate (DMC) (1:2 v/v). The rate performance was measured at the current density sequence of 0.1 C, 0.2 C, 0.5 C, 1.0 C, 2.0 C, 5.0 C, and 0.1 C in the voltage range between 3.0 V and 0.005 V (vs. Li/Li^+) (five cycles each current density, 1 C = 335 mAh/g). The cyclic measurement was carried out at a current density of 0.2 C in the voltage range of 3.0– 0.005 V (vs. Li/Li^+) for 50 rounds. The specific capacity was calculated on the basis of only the active material. The lithiation process was defined as discharging and delithiation process was defined as charging.

Cyclic voltammetry (CV) test was performed on CHI 1040B potentiostat/galvanostat analyzer (Shanghai Chenhua instrument Co., Ltd) at a scanning rate of 0.1 mV/s from 0.005 V to 3 V.

Electrochemical impedance spectroscopy (EIS) measurement was conducted on an Autolab modular electrochemical system (Autolab PGSTAT302N) over a frequency range of 100 kHz to

0.01 Hz after the lithium-ion battery devices were cycled for three rounds at 0.2 C (1 C = 335 mA/g).

3. Results and discussion

The concentration of PS is critical for the formation of TiO_2 microspheres (Fig. 1). With the PS mass concentration of 0 wt% and 4 wt%, only TiO_2 nanoparticles with the average size below 100 nm are obtained (Fig. 1a and b). However, with the PS mass concentration increased to 8 wt%, TiO_2 microspheres with the average size of *ca* 1 μm are generated (Fig. 1c). High magnification SEM image shows that the TiO_2 microspheres are actually formed by the close-packing of TiO_2 nanoparticles with the size of tens of nanometers (inset of Fig. 1c). With the PS mass concentration further increased to 16 wt%, TiO_2 microspheres still exist and the average size does not change significantly (Fig. 1d). It seems that the surface of the microspheres is smoother and the nanoparticles are better packed than the microspheres in Fig. 1c, implying a better templating effect with increased PS concentration. The increasing PS amount introduces more interfacial tension between the dissolved PS and solvent. As a result, a phase transition occurs and PS colloids are formed in solution to reduce the interfacial tension. The formed PS colloids act as template for the integration of titania nanoparticles under solvothermal treatment. As a result, TiO_2/PS hybrid microspheres are formed, which are converted to TiO_2 microspheres via calcination in air.

The role of concentrated HCl on the formation of TiO_2 microspheres is further studied. Fig. 2a shows that without HCl, TiO_2 nanoparticles instead of microspheres are formed. However, when the HCl concentration is increased to 2 wt% or 4 wt%, micrometer sized TiO_2 spheres are formed (Fig. 2b and c). When further increasing the HCl concentration to 8 wt%, the microspheres disappear and TiO_2 nanoparticles are observed again (Fig. 2d). The results show that the TiO_2/PS microspheres are only formed within limited concentration range of the concentrated HCl. In case of insufficient amount of HCl, the interfacial tension between the dissolved PS and solvent is not large enough to induce the formation of PS colloids. As a result, only nanoparticles from the sol–gel reaction of TTIP are obtained. In case of too high amount of HCl, the originally dissolved PS likely precipitates from the solution and still only TiO_2 nanoparticles are formed, due to high surface tension between PS and solvent. Therefore, stable PS colloids only exist within a certain concentration range of the concentrated HCl.

To better understand the morphology change of pure PS in solution with increasing HCl concentration, we spin coat the stock solutions before and after solvothermal treatment on Si substrate. Regarding the samples before calcination, only very few particles are observed without concentrated HCl (Fig. 3a). Nevertheless, with 2 wt% and 4 wt.% of concentrated HCl, particles are formed, which are supposed to be PS (Fig. 3b and c). With the HCl concentration further increased to 8 wt%, particles are still visible, but lamellae like structures appear (Fig. 3d), implying a morphology transition from particles to large sized lamellae in solution due to increased surface tension. The results prove that the pure PS does really form colloids in solution with certain amount of concentrated HCl. The morphologies of PS after solvothermal treatment are shown in Fig. S1, where a similar trend of morphology evolution against the mass concentration of the concentrated HCl is observed. Furthermore, it can be seen that with solvothermal treatment the sizes of the PS particles are increased to a scale comparable to the TiO_2/PS microspheres. The results indicate that the solvothermal treatment promotes the growth of the preliminary formed PS colloids.

The impact of solvothermal treatment on the TiO_2 microspheres is investigated by applying different solvothermal reaction time (from 0 to 8 h). Without solvothermal treatment, bulk lamellae like structures are formed. Only few particles are observed (Fig. 4a). With the solvothermal treatment of 2 h, TiO_2 microspheres are dominantly formed (Fig. 4b). Extending the solvothermal reaction time to 4 h and 8 h, TiO_2 microspheres were still observed and the morphologies did not change significantly (Fig. 4c and d). The results show that the solvothermal treatment is critical for the formation of the TiO_2/PS microspheres. It promotes the integration of TiO_2 nanoparticles into the PS colloids. The integration of TiO_2 nanoparticles conversely stabilizes the PS colloids because permanent continuous Ti–O network within the PS colloids is formed as the sol–gel reaction proceeds.

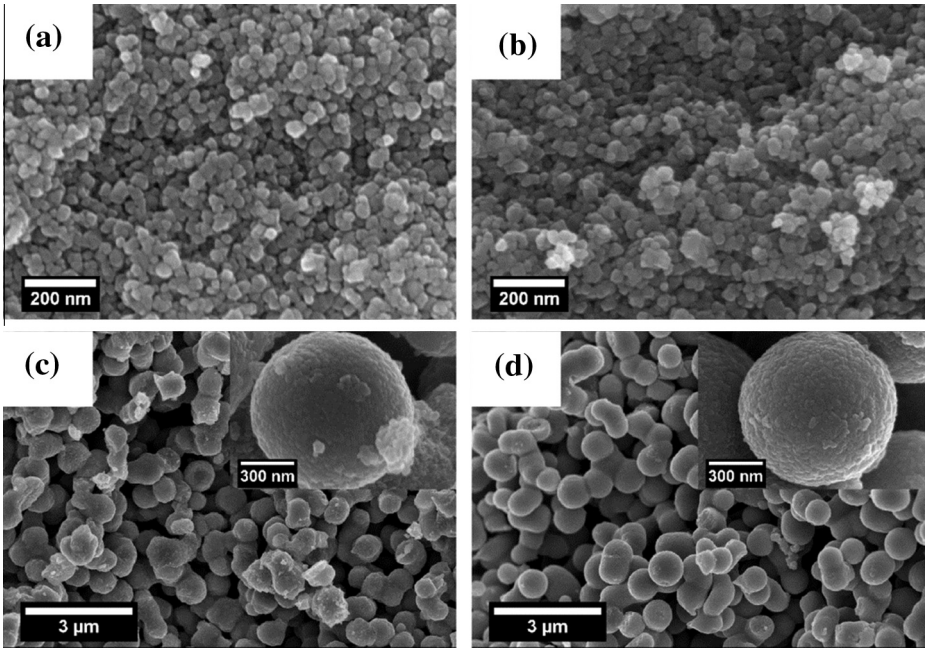

Fig. 1. SEM images of TiO_2 templated by different mass concentrations of PS: 0 wt% (a), 4 wt% (b), 8 wt% (c), and 16 wt% (d) with 2 wt% of concentrated HCl and 8 wt% of TTIP with respect to the mass of DMF. Insets: structure details of the TiO_2 microspheres. Scale bars in image a, b: 200 nm, scale bars in image c, d: 3 μm.

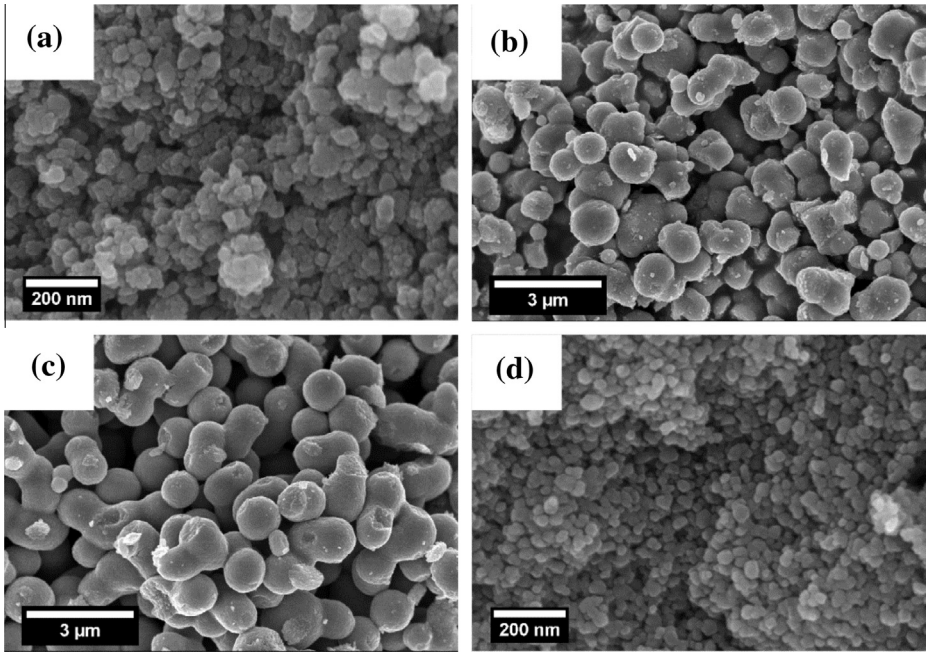

Fig. 2. SEM images of TiO_2 synthesized with different amounts of concentrated HCl: 0 wt% (a), 2 wt% (b), 4 wt% (c), and 8 wt% (d). In addition, 10 wt% of PS and 8 wt% of TTIP with respect to the mass of DMF were present. Scale bars in image a, d: 200 nm, scale bars in image b, c: 3 μm.

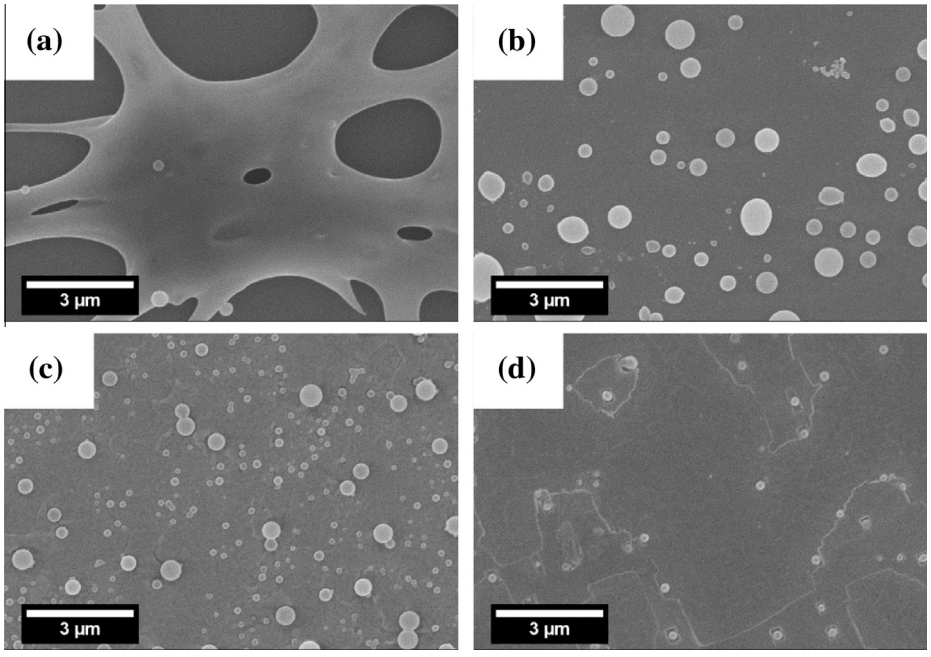

Fig. 3. SEM images of pure PS (before solvothermal treatment) spin coated on Si substrate with different mass concentrations of concentrated HCl: 0 wt% (a), 2 wt% (b), 4 wt% (c), and 8 wt% (d) and 10 wt% of PS with respect to the mass of DMF. Scale bars in image a–d: 3 μm.

To further support the interpretation, an amphiphilic diblock copolymer of polystyrene-*block*-poly (ethylene oxide) (PS-*b*-PEO) was used as a co-templating agent of PS. Fig. 5 shows that with the PS-*b*-PEO mass concentration of 0 wt% and 0.3 wt%, the surface of some TiO_2 microspheres are quite rough, where titania nanoparticles are loosely packed (Fig. 5a and b). Nevertheless, when increasing the PS-*b*-PEO mass concentration to 0.4 wt% and 0.8 wt%, the titania nanoparticles are packed tightly and the surface of the microspheres become quite smooth. Additionally, it is found that when only PS-*b*-PEO is used, TiO_2 nanoparticles instead of microspheres are formed (Fig. S2). The results confirm the synergistic effect of PS and PS-*b*-PEO on the morphology control of the TiO_2 microspheres. PS-*b*-PEO enhances the formation of TiO_2/PS hybrid spheres in the following ways. First, the PEO block of PS-*b*-PEO is an excellent absorber for the titania nanoparticles even under ambient conditions [14]. Second, PS-*b*-PEO can be homogeneously dispersed in the PS homopolymer matrix via a swelling process [52]. Third, under solvothermal treatment, the PS block of PS-*b*-PEO also adsorbs titania nanoparticles as the homopolymer PS does.

The impact of calcination treatment on the morphology, crystallinity, and carbon content of the TiO_2 microspheres has been

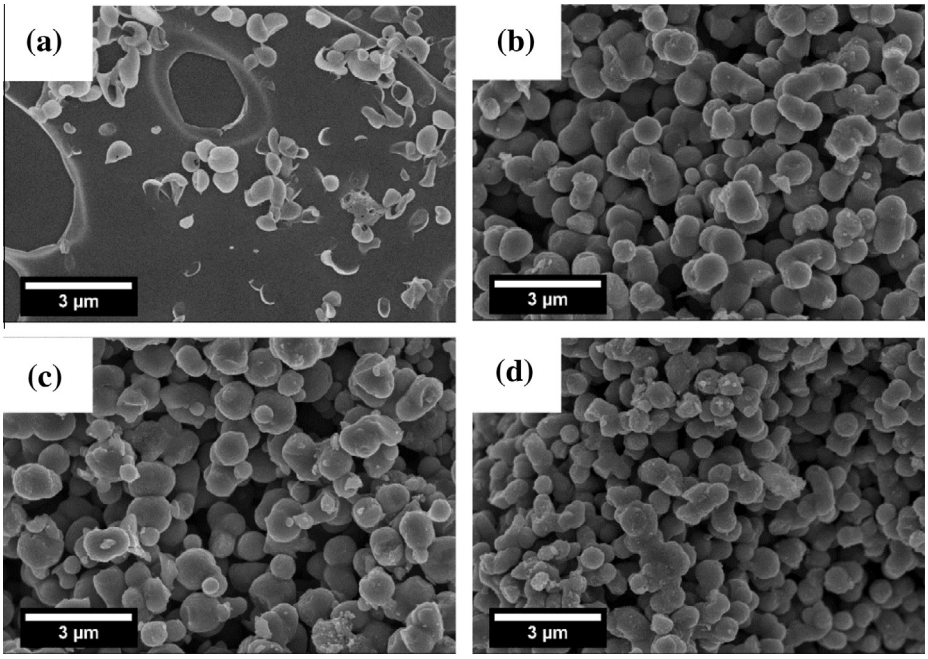

Fig. 4. SEM images of TiO_2 synthesized with different solvothermal reaction time: 0 h (a), 2 h (b), 4 h (c), and 8 h (d) at 110 °C with 2 wt% of conc. HCl, 10 wt% of PS and 8 wt% of TTIP with respect to the mass of DMF. Scale bars in image a–d: 3 μm.

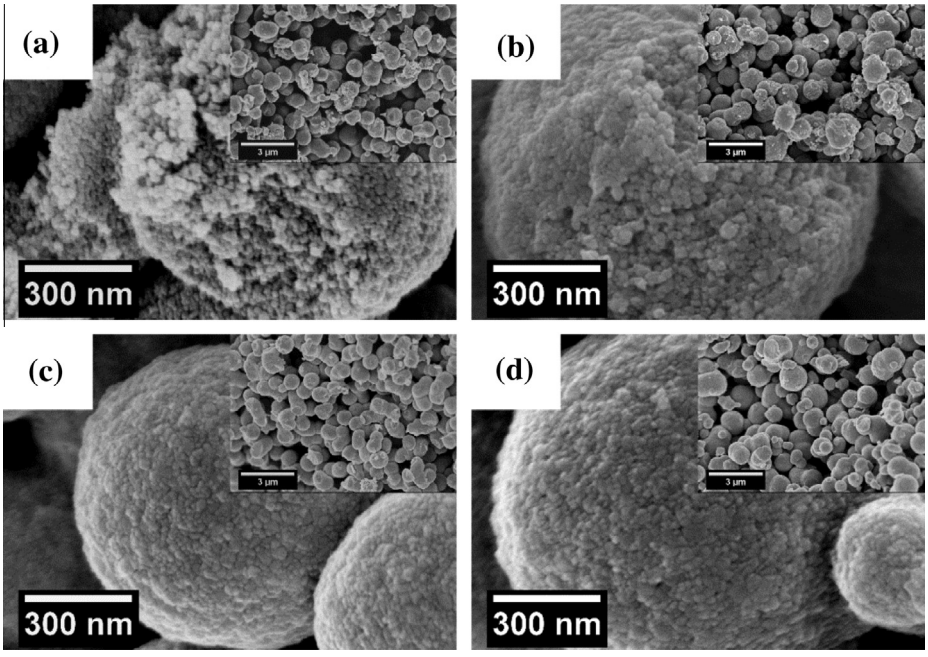

Fig. 5. SEM images of TiO_2 microspheres co-templated by 10 wt% of PS and different mass concentrations of PS-*b*-PEO: 0 wt% (a), 0.3 wt% (b), 0.4 wt% (c), and 0.8 wt% (d) with 2 wt% of conc. HCl and 8 wt% of TTIP with respect to DMF. Scale bars in image a–d: 300 nm.

systematically investigated. Fig. 6 shows that the shape of the microspheres is still retained after calcination, indicating good structure stability of the microspheres. After calcination in argon for 3 h at 500 °C, the average diameter of the microspheres decreases from 1.2 μm ± 0.1 μm to *ca.* 0.93 ± 0.09 μm (Fig. 6a and b). The size reduction originates from the simultaneous carbonization of PS and sintering of the titania species. By further treating the TiO_2/C microspheres with heating in air at 300 °C for 0.5 h and 1.5 h, the averages diameters of the TiO_2/C microspheres are slightly increased to around 1.1 μm (Fig. 6c and d). The microspheres expand when the carbon inside the microspheres is converted to gas during calcination in air. With calcination in air at 500 °C for 3 h, the average size significantly decreases to 0.77 ± 0.03 μm (Fig. 6e). The complete removal of PS is accompanied with the sintering of the titania species, leading to a shrinking. Finally, the tap densities of the bare TiO_2 (only calcination in air) and TiO_2/C microspheres (only calcination in argon) are 1.32 g/cm^3 and 0.87 g/cm^3 respectively, which are quite high compared to normal nanostructured TiO_2 [53].

The TEM results reveal morphology details and local crystallization of the TiO_2/PS and TiO_2/C microspheres (Fig. 7). Local crystallization is hardly observed by high resolution TEM (HRTEM) in the

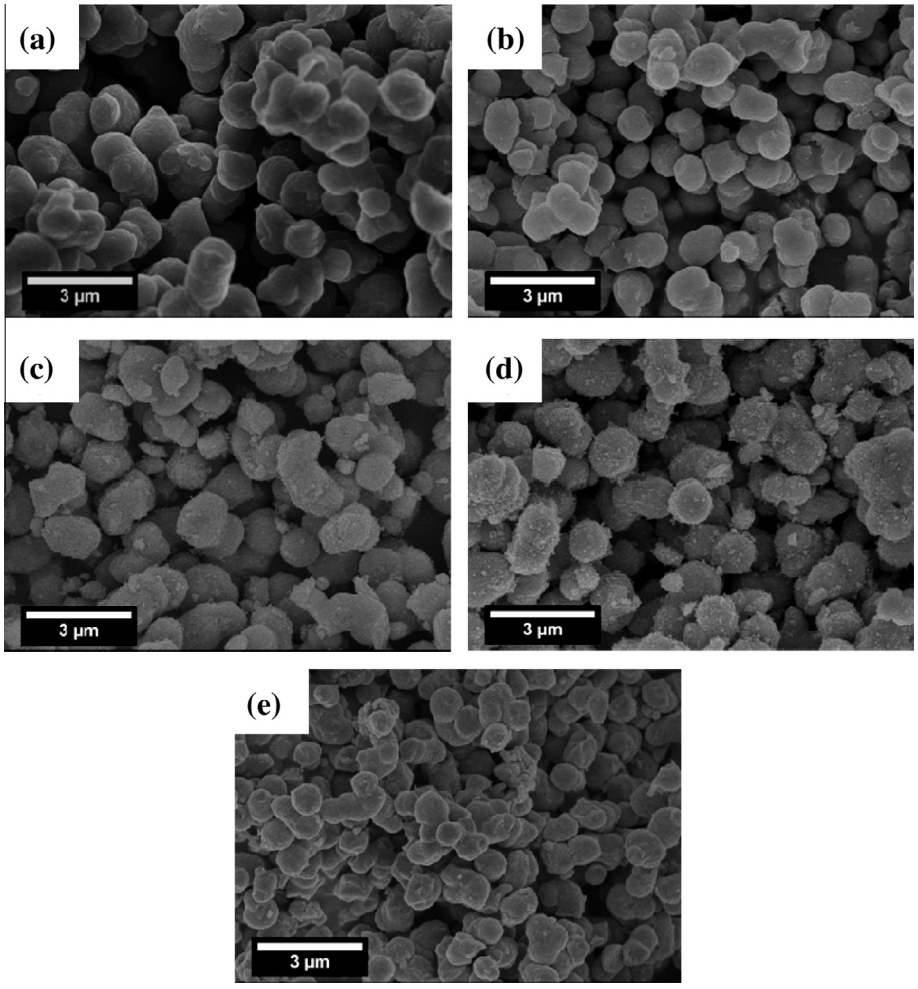

Fig. 6. SEM images of the as-prepared TiO_2/PS microspheres (a), and TiO_2/C hybrid microspheres. Sample details: (b) calcination in argon for 3 h at 500 °C, (c) tandem calcination in argon for 3 h at 500 °C and in air for 0.5 h at 300 °C, (d) tandem calcination in argon for 3 h at 500 °C and in air for 1.5 h at 300 °C, and (e) calcination in air for 3 h at 500 °C. Scale bars in image a–c: 3 μm.

TiO_2/PS microspheres. But the selected area diffraction (SAED) pattern shows that TiO_2 of anatase exists (Fig. 7a and b) It suggests a very poor crystallization of TiO_2 within the TiO_2/PS microspheres. After calcination, voids were observed in the TEM images (Fig. 7c, e, g, and i). Crystal plane of (101) of anatase is observed by the HRTEM images and ring-like scattering features are exhibited in the SAED patterns, indicating the formation of polycrystalline TiO_2 (Fig. 7d, f, h, and j). Besides the typical (101) crystal plane, the high reactive (001) crystal plane is also observed by the HRTEM images (Fig. S3) [54,55]. During solvothermal reaction, small amount of amine is *in situ* formed via the slight decomposition of DMF. The amine acts as capping agent to stabilize the (001) facet through intermolecular interactions. As a result, the (001) facet is retained after solvothermal reaction [56,57].

No clear peaks are observed in the XRD data of the TiO_2/PS microspheres (Fig. 8). The results indicate that the solvothermal treatment only promotes the formation of TiO_2 microspheres, while it does not contribute to the crystallization of TiO_2. It also indicates that crystallization only happens in small local area of the TiO_2/PS microspheres as observed by the SAED (Fig. 7b). After calcination in argon, characteristic scattering peaks are observed, which indicates that the amorphous TiO_2 is converted to anatase. The average size of the nanocrystals is calculated to be *ca.* 8 nm according to the Debye-Scherrer equation based on the (101) peak. With consecutive heating in air at 300 °C for 0.5 h, the width of the (101) peak is significantly narrowed with the average crystal size increased to 12 nm. When the heating time is further extended to 1.5 h, the crystal size does not change significantly. The scattering signal of the (001) crystalline plane is cancelled according to the X-ray extinction rule of the body centered feature of the TiO_2 anatase phase. Therefore, even though the (001) plane is observed by TEM, no corresponding diffraction peak can be exhibited by XRD. The XRD profile of the bare TiO_2 microspheres obtained by calcination in air possesses the most narrow (101) peak with the average crystal size of 28 nm.

The content and nature of carbon within the TiO_2/C microspheres under different calcination conditions are investigated by TGA (Fig. 8b) and Raman spectroscopy (Fig. 8c). After calcination in argon at 500 °C for 3 h, around 8 wt% of carbon exists within the TiO_2/C microspheres. By further treatment with heating in air at 300 °C for 0.5 h and 1.5 h, the carbon content is decreased to 4 wt% and 2 wt% respectively. The Raman spectroscopy data show clear D band and G band within the TiO_2/C microspheres with 8 wt % of carbon, which indicates the presence of both disordered carbon (D band) and graphite-like carbon (G band) originated from the decomposition of PS [58,59]. After further heat treatment in air at 300 °C for 0.5 h, only very weak D band and G band are observed because carbon is partially removed.

The UV–Vis spectra study the light absorption behavior of the TiO_2 microspheres with different carbon contents (Fig. 8d). With

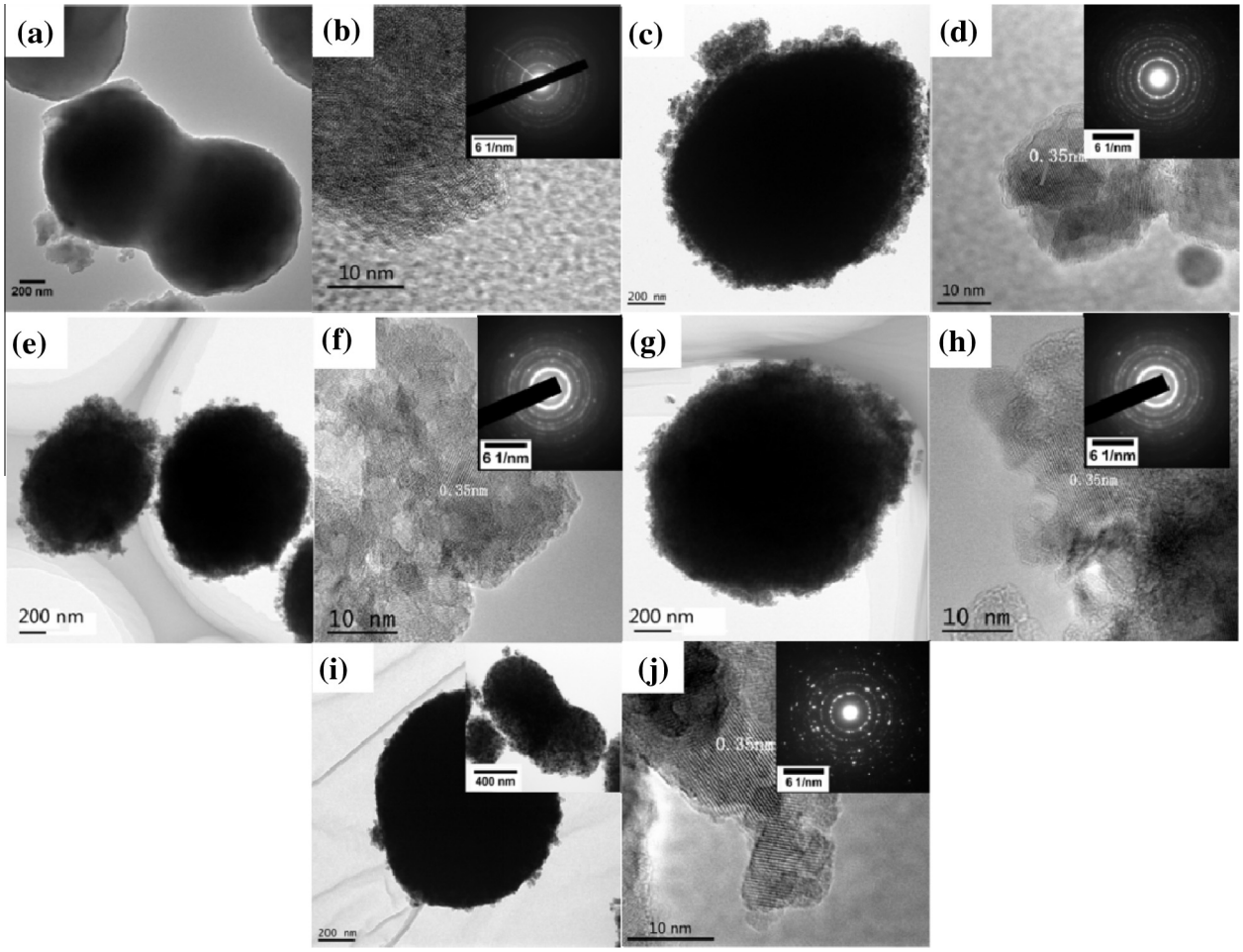

Fig. 7. TEM (a, c, e, g, and i) and HRTEM (b, d, f, h, and j) images of the TiO_2/PS microspheres and TiO_2/C hybrid microspheres. Sample details: (a, b) as-prepared TiO_2/PS microspheres, (c, d) calcination in argon for 3 h at 500 °C, (e, f) tandem calcination in argon for 3 h at 500 °C and in air for 0.5 h at 300 °C, (g, h) tandem calcination in argon for 3 h at 500 °C and in air for 1.5 h at 300 °C, and (i, j) calcination in air for 3 h at 500 °C. Inset in image i: magnified image of the TiO_2 microsphere; insets in image b, d, f, h, and j: selected area electron diffraction (SAED) patterns. Scale bars in image a, c, e, g, and i: 200 nm, scale bars in image b, d, f, h, and j: 10 nm.

8 wt% of carbon, significant visible light absorption is observed due to the presence of decent amount of carbon. With the carbon content reduced to 4 wt% and 2 wt.%, absorption in the visible light range is still present with the absorption threshold at 454 nm and 402 nm respectively [60]. It is important to note that the bare TiO_2 microspheres do not exhibit meaningful absorption in the visible light range with the absorption threshold at 397 nm.

The XPS experiment is applied to examine carbon doping within the TiO_2/C microspheres (Fig. 9). To make a comparison, both, the bare TiO_2 microspheres (0 wt% of carbon, calcination in air) and TiO_2/carbon microspheres (8 wt% of carbon, calcination in argon) are measured by XPS with the same protocol. The high resolution and survey profiles of Ti2p, O1s, and C1s of both bare TiO_2 and TiO_2/C microspheres show very similar results. The peaks located at 458.6 eV and 464.3 eV correspond to the binding energies of Ti 2p3/2 and Ti 2p1/2 (Fig. 9a), indicating the presence of Ti^{4+} in TiO_2. Furthermore, the existence of the symmetric Ti 2p peaks implies the formation of stoichiometric TiO_2 without defects [61]. Regarding the O1s profile, peaks located at 529.9 eV and 531.2 eV are presented (Fig. 9b), which are ascribed to the Ti–O bond (lattice oxygen) and possible hydroxyl group adsorbed on the TiO_2 surface [59]. The C1s profiles of both bare TiO_2 and TiO_2/C microspheres exhibit similar patterns, where a primary peak is located at 284.8 eV. The presence of carbon on the bare TiO_2 microsphere is ascribed to the adventitious carbon adsorbed on the TiO_2 surface. Because the C1s peak of the graphite-like carbon located at 285.0 eV may overlap with the peak at 284.8 eV, it is hard to distinguish the existence of the graphite-like carbon within the TiO_2/C hybrids by analyzing this major peak. However, a very small peak located at 290.9 eV may indicate the presence of graphite-like carbon within the TiO_2/C microspheres [61]. The absence of the peak located at 282.0 eV indicates that no carbon substitutes oxygen in the TiO_2 lattice to form Ti–C bond [62]. By combing the color change phenomenon (Fig. S4), Raman, UV–Vis, and XPS results, it is reasonable to conclude that the doped carbon may be homogeneously distributed in the interstitial sites of the TiO_2 lattice [60].

The pore size distribution, pore volume, and Brunauer–Emmet t–Teller (BET) surface area of the TiO_2 microspheres with different carbon contents are further characterized (Fig. 10). The TiO_2/C microspheres obtained by calcination in argon exhibit a bimodal pore size distribution with the pore sizes of 50 nm and 110 nm respectively (Fig. 10a). When further heating treatment in air is applied, the pores with the size of 50 nm disappear and only the pores with the size of 110 nm are left. It is reasonable to conclude that the pores of 50 nm originate from the *in situ* formed carbon; while the pores of 110 nm can be ascribed to the voids among the TiO_2 nanoparticles. Compared to TiO_2/C, the bare TiO_2 microspheres only show very small portion of pores due to the complete removal of PS and significant densification of the TiO_2 nanoparticles. The bare TiO_2 microspheres exhibit a low pore volume of

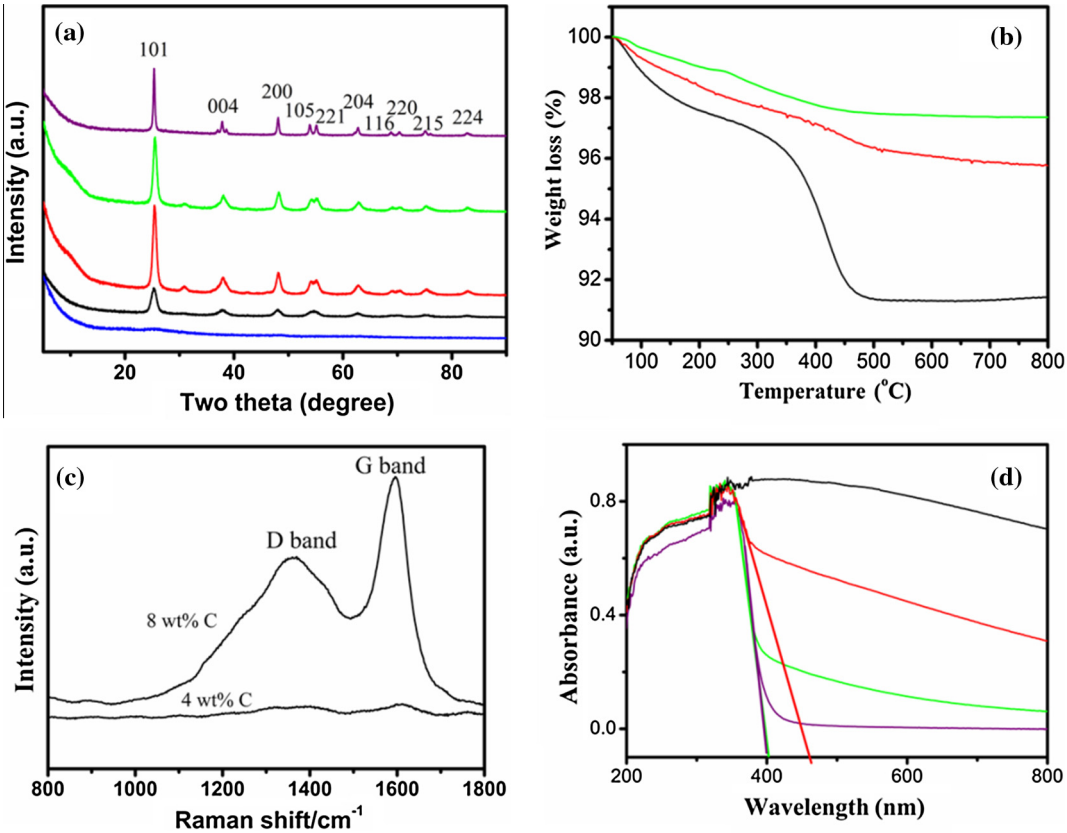

Fig. 8. XRD (a), TGA (b), Raman (c), and UV–Vis (d) spectra of the TiO_2/C hybrid microspheres. Sample details: blue (as-prepared TiO_2/PS microspheres), black (calcination in argon for 3 h at 500 °C), red (tandem calcination in argon for 3 h at 500 °C and in air for 0.5 h at 300 °C), green (tandem calcination in argon for 3 h at 500 °C and in air for 1.5 h at 300 °C), and purple (calcination in air for 3 h at 500 °C). (For interpretation of the references to colour in this figure legend, the reader is referred to the web version of this article.)

0.02 m^3/g, while the TiO_2/C microspheres obtained by calcination in argon possess the pore volume of around 0.18 m^3/g (Fig. 10b). The BET surface area of the TiO_2/C microspheres is 130 m^2/g, which is slightly decreased to 90 m^2/g and 70 m^2/g after further heating treatment in air. Compared to the TiO_2/C microspheres, the bare TiO_2 microspheres only have a very low BET surface area of 12 m^2/g (Fig. 10c). It is worth pointing out that it is common to present individual data point of the specific surface area without error bars [6,63,64]. Furthermore, because the composite after calcination is very homogeneous, it is reasonable to assume that the structure inhomogeneity within the bulk is minimized as shown in the low magnification SEM image (Fig. S5). Therefore, based on the above considerations, it can be concluded that the specific surface area data exhibited by Fig. 10c is representative.

Small angle X-ray scattering (SAXS) is further applied to investigate the characteristic structures within the TiO_2/C nanohybrids. The SAXS data provide average structure information within the bulk in a statistical way [65–67]. Based on the SAXS data (Fig. 11), the existence of the small TiO_2 nanoparticles is confirmed. According to the fitting model, the derived average particle size within the sample calcined in argon is *ca.* 6.4 nm, which originates from the primary TiO_2 particles. Regarding the samples with further heat treatment in air following calcination in argon, the average sizes of the primary particles are slightly increased to around 7.6 nm. However, the average particle size within the TiO_2 microspheres calcined in air is slightly decreased to 5.4 nm, which is supposed to be due to the densification process of the titania species during calcination.

The application of the TiO_2 microspheres as photo catalyst for water splitting has been demonstrated under full spectrum (Fig. 12a) and visible light illumination (Fig. 12b). Compared to the commercial P25 TiO_2 nanoparticles (dark cyan), the bare TiO_2 microspheres show moderate photo catalysis performance (purple). It is supposed to be the consequence of low specific surface area and lack of heterojunction due to the existence of pure anatase [68]. With 2 wt% of carbon, the TiO_2/C microspheres exhibit enhanced photo catalytic performance (green). It is impressive that the performance is even superior to the commercial P25 considering that no highly active heterojunction existing in the TiO_2/C microspheres. The improved property originates from the combined effects of increased specific surface area and pore volume, improved crystallization, existence of high active (001) crystal plane, and enhanced light absorption [55,68]. With further increased carbon content to 4 wt%, the photo catalytic performance starts to decrease (red). The TiO_2/C microspheres with 8 wt% of carbon show the lowest hydrogen conversion efficiency (black). The excessive amount of carbon not only blocks the absorption of light by TiO_2, but also inhibits the transportation of electrons and holes from TiO_2 to water [69,70]. Therefore, an optimized carbon content value exists regarding the photo catalytic performance. Furthermore, the bare TiO_2 microspheres exhibit negligible photo catalytic performance under visible light illumination due to very weak visible light absorption as confirmed by UV–Vis (dark, Fig. 12b). With slightly increased carbon content to 2 wt% (green), distinct visible light the catalytic performance is observed due to increased specific surface area and pore volume, existence of high active (001) crystal plane, and enhanced visible light absorption. But with further increasing carbon content to 4 wt% (red), the efficiency is inversely decreased. With the carbon content of 8 wt% (black), negligible visible light catalytic performance is observed again. The

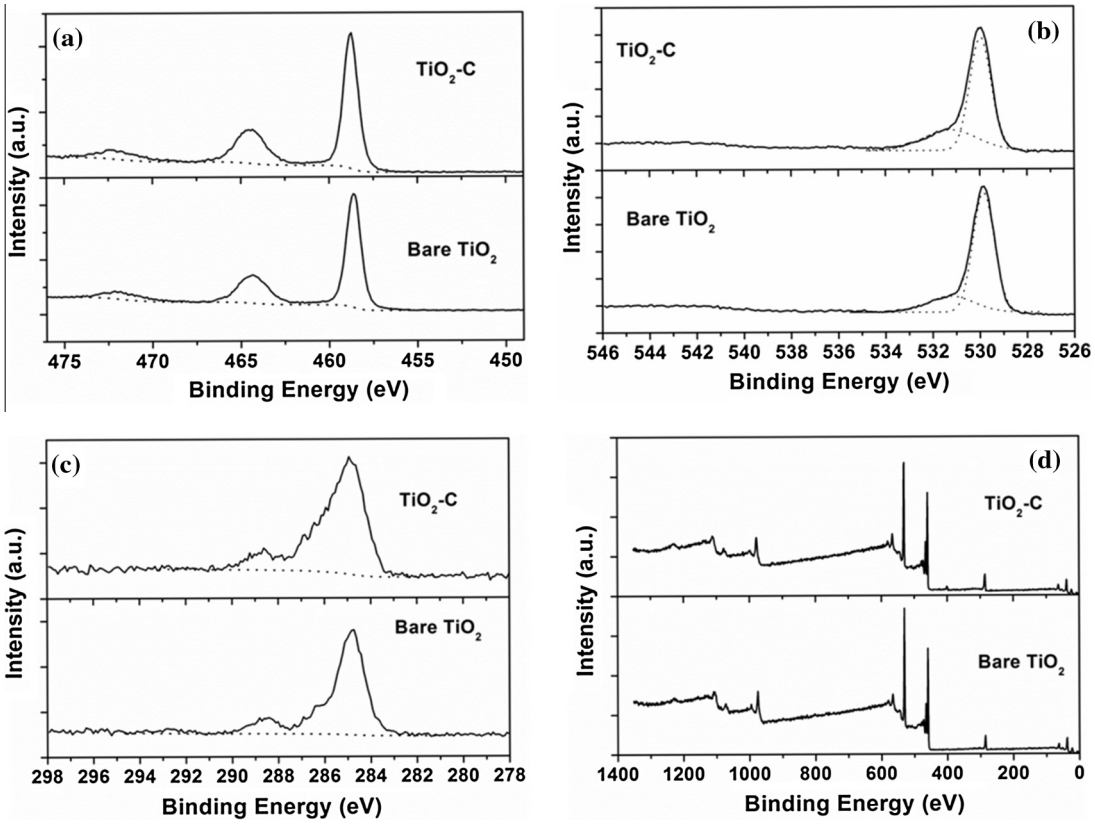

Fig. 9. XPS spectra of the TiO_2/C hybrid microspheres and bare TiO_2 microspheres (a: Ti2p, b: O1s, c: C1s and d: survey). TiO_2/C microspheres: calcination in argon for 3 h at 500 °C (with 8 wt% of carbon by mass). Bare TiO_2 microspheres: calcination in air for 3 h at 500 °C (0 wt% of carbon by mass). Dotted lines in image b: Gaussian fitting curves.

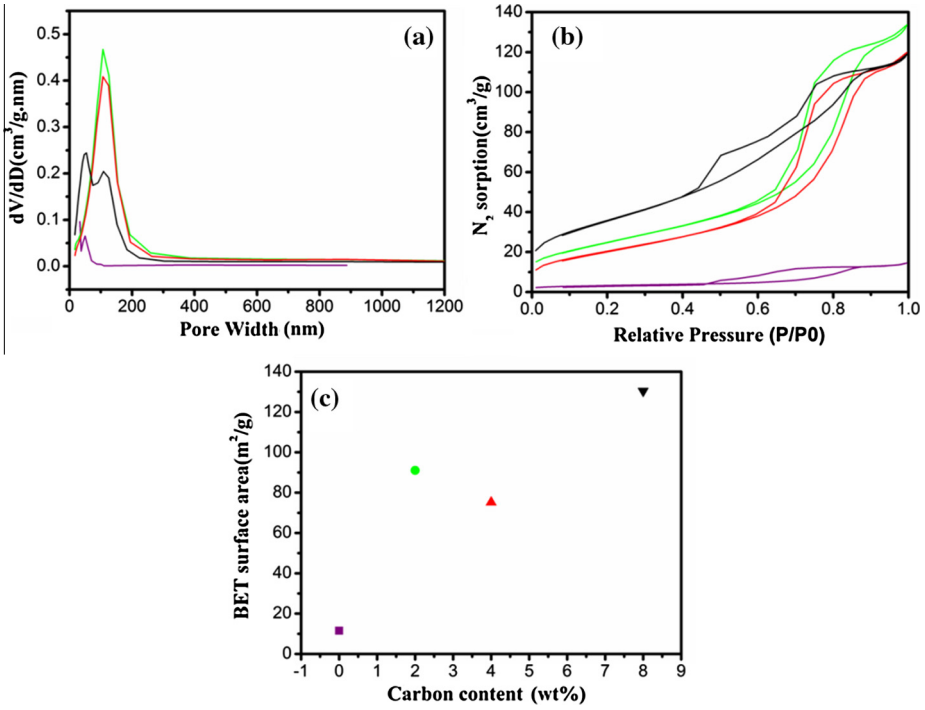

Fig. 10. Pore size distribution (a), N_2 sorption isotherm (b), and BET surface area (c) of the TiO_2/C hybrid microspheres. Sample details: black (calcination in argon for 3 h at 500 °C, 8 wt% of carbon by mass), red (tandem calcination in argon for 3 h at 500 °C and in air for 0.5 h at 300 °C, 4 wt% of carbon by mass), green (tandem calcination in argon for 3 h at 500 °C and in air for 1.5 h at 300 °C, 2 wt% of carbon by mass), and purple (calcination in air for 3 h at 500 °C, 0 wt% of carbon by mass). (For interpretation of the references to colour in this figure legend, the reader is referred to the web version of this article.)

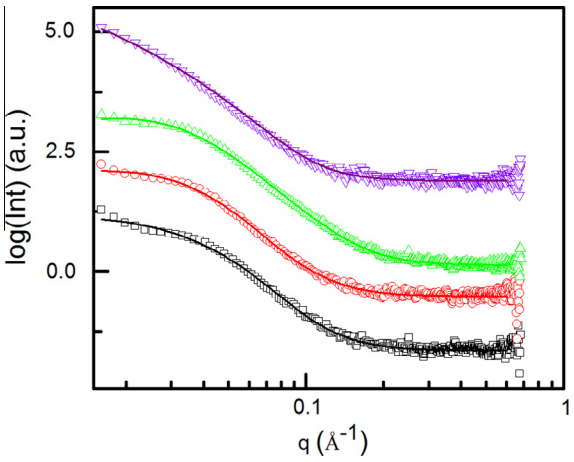

Fig. 11. Integrated SAXS data (points) with model fits (lines) of the TiO_2/C hybrid microspheres. Sample details: black (calcination in argon for 3 h at 500 °C, 8 wt% of carbon by mass), red (tandem calcination in argon for 3 h at 500 °C and in air for 0.5 h at 300 °C, 4 wt% of carbon by mass), green (tandem calcination in argon for 3 h at 500 °C and in air for 1.5 h at 300 °C, 2 wt% of carbon by mass), and purple (calcination in air for 3 h at 500 °C, 0 wt% of carbon by mass). (For interpretation of the references to colour in this figure legend, the reader is referred to the web version of this article.)

results imply that the excessive amount of carbon also significantly inhibits the photo catalysis process under visible light illumination. According to the photoluminescence spectroscopy (Fig. S6), all of the four samples exhibit similar photoluminescence patterns. It implies that the incorporation of carbon does not modify the principle photoluminescence mechanism of the TiO_2 significantly. The multiple peaks by Gaussian fitting indicate that the peaks are located at 460 nm, 486 nm, 499 nm, 529 nm, 541 nm, and 618 nm. While the peak located at 499 nm is ascribed to the state transition within the TiO_2 lattice, the emission at 460 nm, 486 nm, 529 nm, 541 nm, and 618 nm are related to the oxygen vacancies of the TiO_2 [71,72]. Besides the position of the peaks, the intensities of the photoluminescence vary with respect to the carbon content. The bare TiO_2 microspheres exhibit the strongest photoluminescence because the absence of carbon effectively limits the energy dissipation from the excited states. It agrees well with the negligible photo catalytic performance of the bare TiO_2 microspheres. With incorporation of carbon, the intensity of the photoluminescence is decreased because the carbon matrix acts as a potential energy dissipation medium for the excited states of TiO_2. Nevertheless, the relative high photoluminescence of the TiO_2/C hybrid microspheres containing 2 wt% of carbon compared to other TiO_2/C samples implies that the superior outstanding photo catalytic performance may originate from the high specific surface area and enhanced light absorption. It is not only determined by the intrinsic charge separation process.

Besides acting as photo catalyst in the water splitting experiment, the application of the TiO_2 microspheres as lithium-ion battery anode has also been investigated. The discharge/charge curves at 0.2 C (1 C = 335 mAh/g) of the TiO_2 microspheres and TiO_2/C hybrid microspheres are displayed in Fig. 13. Because the carbon content is varied among the samples, the discharge/charge voltage range is set between 3 V and 0.005 V to count the contribution from the carbon as well. Compared to the initial discharge capacity of the bare TiO_2 microspheres (170 mAh/g, Fig. 13a), the initial discharge capacity of the TiO_2/C microsphere with 8 wt% of carbon is more than doubled to 381 mAh/g (Fig. 13b). With decreasing carbon content, the initial discharge capacity is slightly reduced to 300 mAh/g (4 wt% of carbon, Fig. 13c) and 234 mAh/g (2 wt% of carbon, Fig. 13d). While the initial charge capacity of the bare TiO_2 microsphere is only 85 mAh/g, the initial charge capacity of the TiO_2/C hybrid microspheres with 8 wt% of carbon is almost two and a half times of the TiO_2 microsphere (204 mAh/g). The initial charge capacities of the TiO_2/C microspheres with decreased carbon content are 156 mAh/g (4 wt% of carbon) and 127 mAh/g (2 wt% of carbon) respectively. Compared to the initial coulombic efficiency of bare TiO_2 microspheres (50%), the coulombic efficiencies of the TiO_2/C hybrid microspheres are slightly improved (from 52% to 54%). The second discharge/charge capacities of the TiO_2 microsphere are decreased to 81 mAh/g. But the second discharge/charge capacities of the TiO_2/C microspheres with 8 wt% of carbon are still 237 mAh/g and 207 mAh/g respectively. Correspondingly, the TiO_2/C microspheres with 4 wt% and 2 wt% of carbon still exhibit better performance than the bare TiO_2 microspheres. The fifth discharge/charge capacities of both the TiO_2 and TiO_2/C microspheres do not change significantly with respect to each 2nd cycle. Even though the 50th discharge/charge capacities of the TiO_2 microspheres are slightly increased to 100 mAh/g, the 50th discharge/charge capacities of the TiO_2/C microspheres with 8 wt% of carbon are still two times of the TiO_2 spheres (*ca.* 200 mAh/g). The TiO_2/C microspheres with 4 wt% of carbon show slightly better capacities than the bare TiO_2; while the TiO_2/C microspheres with 2 wt% of carbon exhibit similar capacities to the bare TiO_2. It is also found that along with increased cycles, the discharge plateau of TiO_2 is gradually weakened, which is confirmed by the cyclic voltammetry test (Fig. 14). The cyclic voltammetry test indicates the formation of solid electrolyte interface (SEI) during the first cycle. Besides, the anodic peak of TiO_2 is dramatically weakened after the first cycle. It

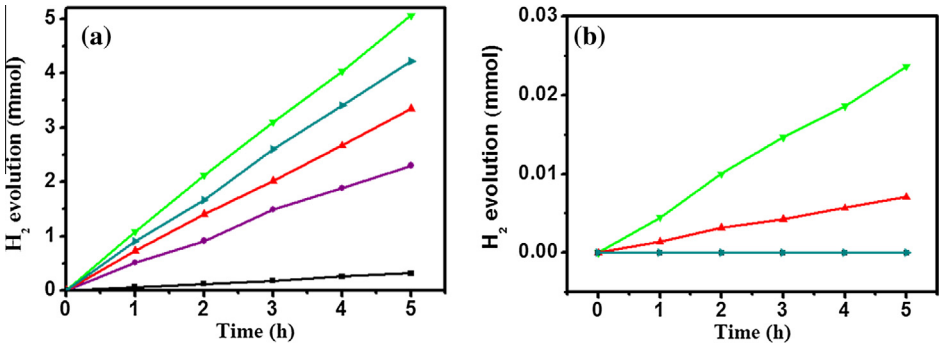

Fig. 12. Hydrogen evolution curves under UV (a) and visible light (UV cut at 420 nm, b) using the TiO_2/C hybrid microspheres as photo catalysts. Sample details are for black (calcination in argon for 3 h at 500 °C, 8 wt% of carbon by mass), red (tandem calcination in argon for 3 h at 500 °C and in air for 0.5 h at 300 °C, 4 wt% of carbon by mass), green (tandem calcination in argon for 3 h at 500 °C and in air for 1.5 h at 300 °C, 2 wt% of carbon by mass), purple (calcination in air for 3 h at 500 °C, 0 wt% of carbon by mass), and dark cyan (commercial P25 TiO_2 nanoparticles). (For interpretation of the references to colour in this figure legend, the reader is referred to the web version of this article.)

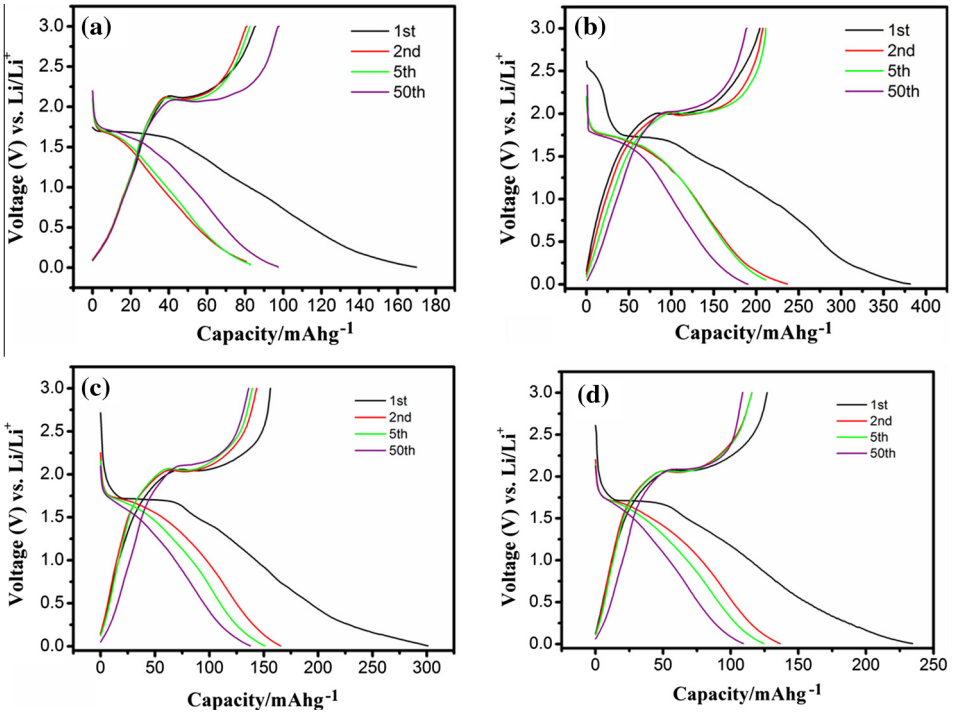

Fig. 13. Discharge-charge curves of the TiO_2 (a) and TiO_2/C (b, c, and d) hybrid microspheres as lithium-ion battery anodes. Sample details are a: (calcination in air for 3 h at 500 °C, 0 wt% of carbon by mass), b: (calcination in argon for 3 h at 500 °C, 8 wt% of carbon by mass), c: (tandem calcination in argon for 3 h at 500 °C and in air for 0.5 h at 300 °C, 4 wt% of carbon by mass), and d: (tandem calcination in argon for 3 h at 500 °C and in air for 1.5 h at 300 °C, 2 wt% of carbon by mass).

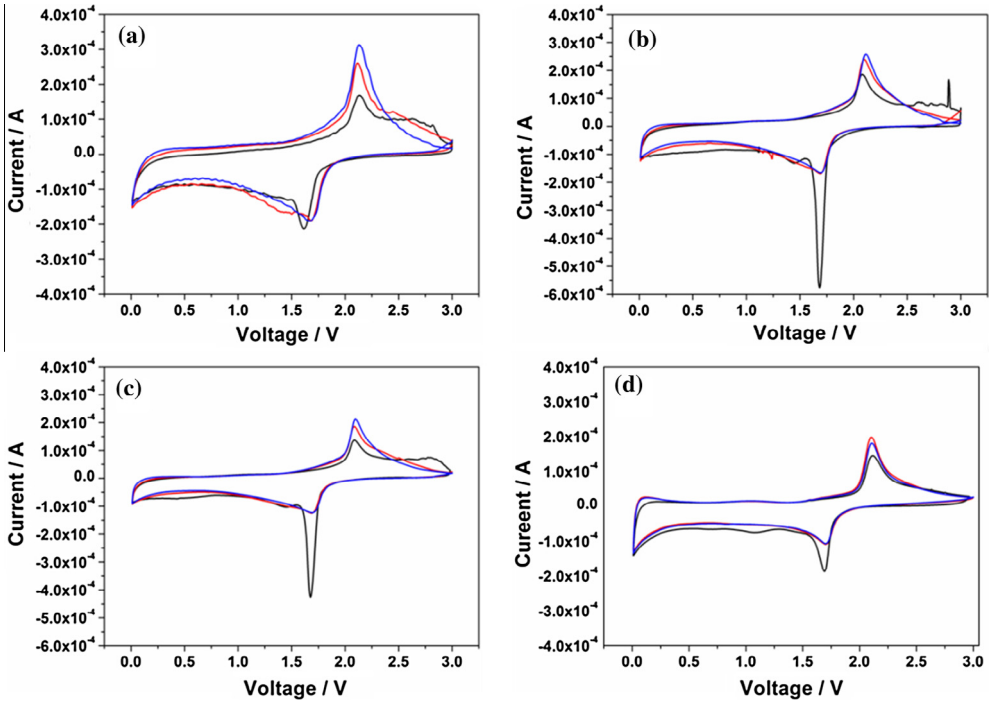

Fig. 14. Cyclic voltammetry profiles of the TiO_2/C hybrid microspheres as lithium-ion battery anodes with different carbon contents. Sample details are a: (calcination in argon for 3 h at 500 °C, 8 wt% of carbon by mass), b: (tandem calcination in argon for 3 h at 500 °C and in air for 0.5 h at 300 °C, 4 wt% of carbon by mass), c: (tandem calcination in argon for 3 h at 500 °C and in air for 1.5 h at 300 °C, 2 wt% of carbon by mass), and d: (calcination in air for 3 h at 500 °C, 0 wt% of carbon by mass).

implies that the structure/crystallinity of TiO_2 have been modified after cycling test. The discharge/charge results indicate that the capacities are increased with increasing amount of carbon. Considering that the capacity is more than doubled with only 8 wt% of carbon, it is reasonable to say that the increased capacity is not only contributed by the carbon itself, but also from the TiO_2 [26,73,74]. The presence of carbon effectively improves the electrochemical property of the TiO_2 nanoparticles. On the one hand, the specific surface area and pore volume of the TiO_2/C microspheres are dramatically increased compared to the bare TiO_2 micro-

spheres. On the other hand, the existence of carbon is supposed to improve the electron conductivity of TiO_2, leading to better electrochemical kinetics than the bare TiO_2. Compared to the reported electrochemical performance of the TiO_2 LIB anode, the capacity is lower in the voltage range between 3.0 V and 1.0 V [75]. It indicates that only partial lithiation of TiO_2 happens during the discharging process. It is probably due to the fact that no anisotropic low-dimensional TiO_2 nanostructures are present in the hybrid microspheres. Instead, only solid TiO_2 nanoparticles exist, which may lead to inferior lithiation/delithiation kinetics. Furthermore, there is no essential porosity within the TiO_2 framework, which also limits the electrochemical performance of TiO_2 [1,75,76]. Fig. 15a to 15d exhibit the detailed cyclic performance of the TiO_2/C hybrid microspheres with different carbon contents. The figures show that the TiO_2/C microspheres with 8 wt% of carbon possess the most stable cyclic performance compared to other samples. The results suggest the carbon matrix helps to stabilize the hierarchical structures and corresponding electrochemical performance. The rate performance of the TiO_2 and TiO_2/C microspheres are exhibited in Fig. 15e. At different rates, the discharge/charge capacities of the TiO_2/C microspheres are higher than the capacities of the bare TiO_2 microspheres due to high specific surface area and improved electron conductivity. However, the difference is narrowed with increasing rate, which is almost minimized at 5 C (*ca.* 40 mAh/g). The capacities of the TiO_2/C and TiO_2 microspheres are recovered to *ca.* 213 mAh/g and 137 mAh/g at 0.1 C respectively, indicating a good structure stability of both the TiO_2 and TiO_2/C microspheres during repeated charge and discharge processes. The electrochemical impedance spectroscopy (EIS) measurement shows that the TiO_2/C hybrid anode possesses smaller charge transfer resistance compared to the bare TiO_2 anode (Fig. 16). Particularly, the TiO_2/C anode with 8 wt% of carbon exhibits the smallest charge transfer resistance compared with the samples with lower carbon contents (4.6 Ω vs. *ca.* 37 Ω). The EIS results further prove that the TiO_2/C hybrid anodes with higher carbon content exhibit better rate performance.

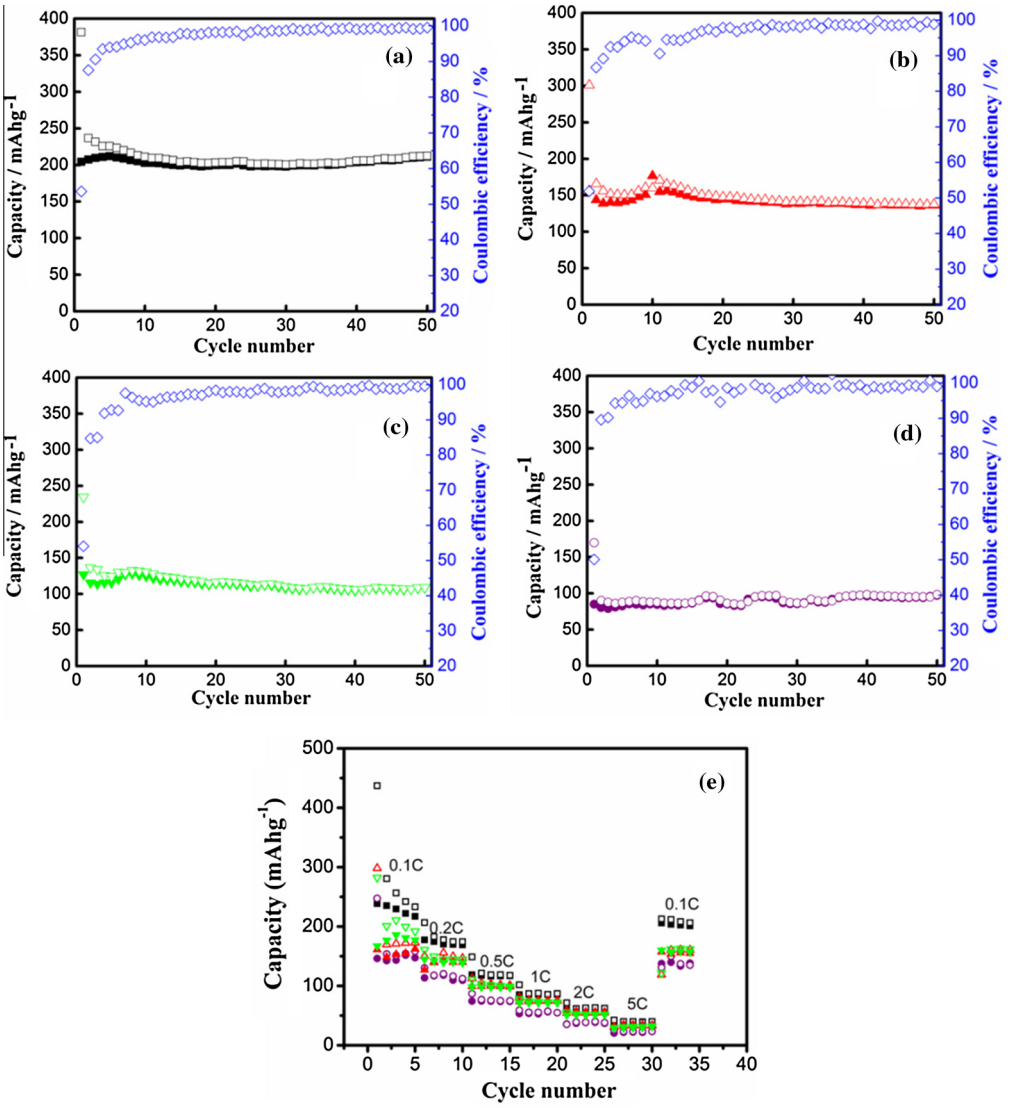

Fig. 15. Cyclic (a–d) and rate (e) performance of the TiO_2/C hybrid microsphere lithium-ion battery anodes with different carbon contents. Figure details: image a & black symbols in image e (calcination in argon for 3 h at 500 °C, 8 wt% of carbon by mass), image b & red symbols in image e (tandem calcination in argon for 3 h at 500 °C and in air for 0.5 h at 300 °C, 4 wt% of carbon by mass), image c & green symbols in image e (tandem calcination in argon for 3 h at 500 °C and in air for 1.5 h at 300 °C, 2 wt% of carbon by mass), and image d & purple symbols in image e (calcination in air for 3 h at 500 °C, 0 wt% of carbon by mass). Open symbols: discharge, solid symbols: charge. Blue squares in image a–d: coulombic efficiency of each cycle. (For interpretation of the references to colour in this figure legend, the reader is referred to the web version of this article.)

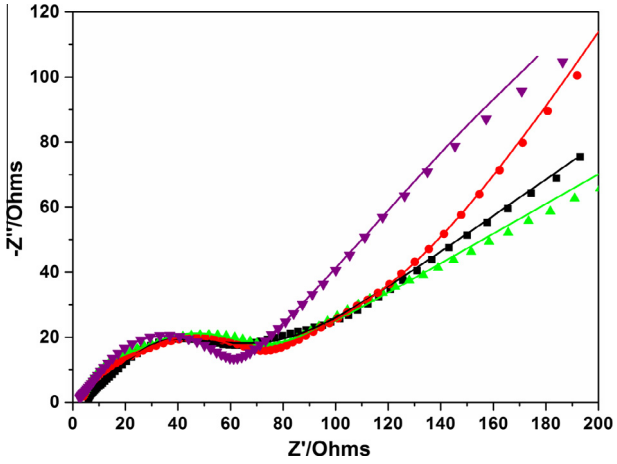

Fig. 16. Experimental (symbol) and fitted (line) electrochemical impedance spectroscopy of the TiO_2/C hybrid microspheres as lithium-ion battery anodes. Sample details are black (calcination in argon for 3 h at 500 °C, 8 wt% of carbon by mass), red (tandem calcination in argon for 3 h at 500 °C and in air for 0.5 h at 300 °C, 4 wt % of carbon by mass), green (tandem calcination in argon for 3 h at 500 °C and in air for 1.5 h at 300 °C, 2 wt% of carbon by mass), and purple (calcination in air for 3 h at 500 °C, 0 wt% of carbon by mass). (For interpretation of the references to colour in this figure legend, the reader is referred to the web version of this article.)

4. Conclusions

A new strategy to the solvothermal synthesis of hierarchical porous TiO_2/C hybrid microspheres has been developed. Unlike conventional hydrophilic polymer templating agent, the *in situ* formed hydrophobic polystyrene colloids are employed as a templating agent and carbon source in this work. It circumvents the pre-synthesis of well-defined polystyrene beads and two-phase templating reaction process. The carbon content is systematically tuned between 0 wt.% and 8 wt% by modifying the calcination protocol. Enhanced visible light absorption is achieved with the incorporation of carbon within the TiO_2 microspheres. Significantly increased specific surface area and pore volume portion are also observed in the TiO_2/C microspheres. The TiO_2/C microspheres with 2 wt% of carbon exhibit outstanding photo catalytic performance under full spectrum and visible light illumination, which is superior to the commercial P25 TiO_2 nanoparticles [13]. It is the combined effects of increased surface area and pore volume, improved crystallization, existence of high active (001) crystal plane, and enhanced light absorption. Besides the photo catalytic water splitting experiment, the lithium-ion battery test shows that the TiO_2/C hybrid microsphere anodes exhibit better performance compared to the bare TiO_2 microspheres due to increased surface area and improved electron conductivity from the *in situ* formed carbon [73].

The results reported in this work prove the new concept that hydrophobic polymers can also be utilized as a templating agent to synthesize hierarchical TiO_2 microspheres via the *in situ* formed PS colloid process. It has greatly expanded the scope of the potential templating systems for the synthesis of inorganic functional materials. Future studies on the templating capability of different hydrophobic templating polymers, synthesis and application of other inorganic functional materials are in progress and will be addressed in future publications.

Acknowledgements

This research is funded by the Natural Science Foundation of China (51103172), the Zhejiang Non-profit Technology Applied Research Program (2013C33190), the open project of the Beijing National Laboratory for Molecular Science (20140138), and the External Cooperation Program of Chinese Academy of Sciences (174433KYSB20150013) and Ningbo Key Laboratory of Polymer Materials. S.X. acknowledges the China Scholarship Council (CSC) and P.M-B acknowledges funding by the Center for NanoScience (CeNS) Munich. Help with the synthesis of block copolymer of PS-*b*-PEO from Thomas Wagner, and Jürgen Thiel is greatly appreciated.

Appendix A. Supplementary material

Supplementary data associated with this article can be found, in the online version, at http://dx.doi.org/10.1016/j.jcis.2016.02.032.

Reference

[1] Z.H. Chen, I. Belharouak, Y.K. Sun, K. Amine, Titanium-based anode materials for safe lithium-ion batteries, Adv. Funct. Mater. 23 (2013) 959–969.
[2] X.B. Chen, C. Li, M. Gratzel, R. Kostecki, S.S. Mao, Nanomaterials for renewable energy production and storage, Chem. Soc. Rev. 41 (2012) 7909–7937.
[3] T. Froschl, U. Hormann, P. Kubiak, G. Kucerova, M. Pfanzelt, C.K. Weiss, R.J. Behm, N. Husing, U. Kaiser, K. Landfester, M. Wohlfahrt-Mehrens, High surface area crystalline titanium dioxide: potential and limits in electrochemical energy storage and catalysis, Chem. Soc. Rev. 41 (2012) 5313–5360.
[4] Y. Bai, I. Mora-Sero, F. De Angelis, J. Bisquert, P. Wang, Titanium dioxide nanomaterials for photovoltaic applications, Chem. Rev. 114 (2014) 10095–10130.
[5] J. Bai, B. Zhou, Titanium dioxide nanomaterials for sensor applications, Chem. Rev. 114 (2014) 10131–10176.
[6] E. Madej, F. La Mantia, W. Schuhmann, E. Ventosa, Impact of the specific surface area on the memory effect in li-ion batteries: The case of anatase TiO_2, Adv. Energy Mater. 4 (2014).
[7] M. Rawolle, M.A. Niedermeier, G. Kaune, J. Perlich, P. Lellig, M. Memesa, Y.J. Cheng, J.S. Gutmann, P. Muller-Buschbaum, Fabrication and characterization of nanostructured titania films with integrated function from inorganic-organic hybrid materials, Chem. Soc. Rev. 41 (2012) 5131–5142.
[8] M. Wagemaker, F.M. Mulder, Properties and promises of nanosized insertion materials for li-ion batteries, Acc. Chem. Res. 46 (2013) 1206–1215.
[9] S. Xin, Y.G. Guo, L.J. Wan, Nanocarbon networks for advanced rechargeable lithium batteries, Acc. Chem. Res. 45 (2012) 1759–1769.
[10] D. Grosso, F. Ribot, C. Boissiere, C. Sanchez, Molecular and supramolecular dynamics of hybrid organic–inorganic interfaces for the rational construction of advanced hybrid nanomaterials, Chem. Soc. Rev. 40 (2011) 829–848.
[11] C. Sanchez, P. Belleville, M. Popall, L. Nicole, Applications of advanced hybrid organic–inorganic nanomaterials: from laboratory to market, Chem. Soc. Rev. 40 (2011) 696–753.
[12] F. De Angelis, C. Di Valentin, S. Fantacci, A. Vittadini, A. Selloni, Theoretical studies on anatase and less common TiO_2 phases: Bulk, surfaces, and nanomaterials, Chem. Rev. 114 (2014) 9708–9753.
[13] J.C. Bear, V. Gomez, N.S. Kefallinos, J.D. McGettrick, A.R. Barron, C.W. Dunnill, Anatase/rutile bi-phasic titanium dioxide nanoparticles for photocatalytic applications enhanced by nitrogen doping and platinum nano-islands, J. Colloid Interface Sci. 460 (2015) 29–35.
[14] Y.J. Cheng, J.S. Gutmann, Morphology phase diagram of ultrathin anatase TiO_2 films templated by a single PS-*b*-PEO block copolymer, J. Am. Chem. Soc. 128 (2006) 4658–4674.
[15] D.H. Chen, R.A. Caruso, Recent progress in the synthesis of spherical titania nanostructures and their applications, Adv. Funct. Mater. 23 (2013) 1356–1374.
[16] P.G. Bruce, B. Scrosati, J.M. Tarascon, Nanomaterials for rechargeable lithium batteries, Angew. Chem. Int. Ed. 47 (2008) 2930–2946.
[17] H.-E. Wang, J. Jin, Y. Cai, J.-M. Xu, D.-S. Chen, X.-F. Zheng, Z. Deng, Y. Li, I. Bello, B.-L. Su, Facile and fast synthesis of porous TiO_2 spheres for use in lithium ion batteries, J. Colloid Interface Sci. 417 (2014) 144–151.
[18] Y. Qu, X. Duan, Progress, challenge and perspective of heterogeneous photocatalysts, Chem. Soc. Rev. 42 (2013) 2568–2580.
[19] Z.-Y. Zhou, N. Tian, J.-T. Li, I. Broadwell, S.-G. Sun, Nanomaterials of high surface energy with exceptional properties in catalysis and energy storage, Chem. Soc. Rev. 40 (2011) 4167–4185.
[20] J. Cao, L. Wang, X.M. He, M. Fang, J. Gao, J.J. Li, L.F. Deng, H. Chen, G.Y. Tian, J.L. Wang, S.S. Fan, In situ prepared nano-crystalline TiO_2–poly(methyl methacrylate) hybrid enhanced composite polymer electrolyte for Li-ion batteries, J. Mater. Chem. A 1 (2013) 5955–5961.
[21] K. Hemalatha, A.S. Prakash, K. Guruprakash, M. Jayakumar, TiO_2 coated carbon nanotubes for electrochemical energy storage, J. Mater. Chem. A 2 (2014) 1757–1766.
[22] J. Zhang, F.-X. Xiao, G. Xiao, B. Liu, Self-assembly of a Ag nanoparticle-modified and graphene-wrapped TiO_2 nanobelt ternary heterostructure: surface charge tuning toward efficient photocatalysis, Nanoscale 6 (2014) 11293–11302.
[23] C. Lin, Y. Song, L. Cao, S. Chen, Effective photocatalysis of functional nanocomposites based on carbon and TiO_2 nanoparticles, Nanoscale 5 (2013) 4986–4992.

[24] Z. Zhang, W. Yang, X. Zou, F. Xu, X. Wang, B. Zhang, J. Tang, One-pot, solvothermal synthesis of TiO_2-graphene composite nanosheets, J. Colloid Interface Sci. 386 (2012) 198–204.

[25] Y.D. Liu, J. Goebl, Y.D. Yin, Templated synthesis of nanostructured materials, Chem. Soc. Rev. 42 (2013) 2610–2653.

[26] B. Liu, L.M. Liu, X.F. Lang, H.Y. Wang, X.W. Lou, E.S. Aydil, Doping high-surface-area mesoporous TiO_2 microspheres with carbonate for visible light hydrogen production, Energy Environ. Sci. 7 (2014) 2592–2597.

[27] Y. Ren, Z. Ma, P.G. Bruce, Ordered mesoporous metal oxides: synthesis and applications, Chem. Soc. Rev. 41 (2012) 4909–4927.

[28] J.S. Chen, Y.N. Liang, Y.M. Li, Q.Y. Yan, X. Hu, H_2O–EG-assisted synthesis of uniform urchinlike rutile TiO_2 with superior lithium storage properties, ACS Appl. Mater. Interfaces 5 (2013) 9998–10003.

[29] D.H. Chen, L. Cao, F.Z. Huang, P. Imperia, Y.B. Cheng, R.A. Caruso, Synthesis of monodisperse mesoporous titania beads with controllable diameter, high surface areas, and variable pore diameters (14–23 nm), J. Am. Chem. Soc. 132 (2010) 4438–4444.

[30] P. Lu, Y.N. Xia, Novel nanostructures of rutile fabricated by templating against yarns of polystyrene nanofibrils and their catalytic applications, ACS Appl. Mater. Interfaces 5 (2013) 6391–6399.

[31] D.H. Chen, F.Z. Huang, Y.B. Cheng, R.A. Caruso, Mesoporous anatase TiO_2 beads with high surface areas and controllable pore sizes: A superior candidate for high-performance dye-sensitized solar cells, Adv. Mater. 21 (2009) 2206–2210.

[32] U. Meyer, A. Larsson, H.P. Hentze, R.A. Caruso, Templating of porous polymeric beads to form porous silica and titania spheres, Adv. Mater. 14 (2002) 1768–1772.

[33] Z.Y. Wang, L. Zhou, X.W. Lou, Metal oxide hollow nanostructures for lithium-ion batteries, Adv. Mater. 24 (2012) 1903–1911.

[34] J. Hu, M. Chen, X.S. Fang, L.W. Wu, Fabrication and application of inorganic hollow spheres, Chem. Soc. Rev. 40 (2011) 5472–5491.

[35] J.Y. Liao, B.X. Lei, D.B. Kuang, C.Y. Su, Tri-functional hierarchical TiO_2 spheres consisting of anatase nanorods and nanoparticles for high efficiency dye-sensitized solar cells, Energy Environ. Sci. 4 (2011) 4079–4085.

[36] J.S. Chen, Y.L. Tan, C.M. Li, Y.L. Cheah, D.Y. Luan, S. Madhavi, F.Y.C. Boey, L.A. Archer, X.W. Lou, Constructing hierarchical spheres from large ultrathin anatase TiO_2 nanosheets with nearly 100% exposed (001) facets for fast reversible lithium storage, J. Am. Chem. Soc. 132 (2010) 6124–6130.

[37] Z.Q. Sun, J.H. Kim, Y. Zhao, F. Bijarbooneh, V. Malgras, Y. Lee, Y.M. Kang, S.X. Dou, Rational design of 3D dendritic TiO_2 nanostructures with favorable architectures, J. Am. Chem. Soc. 133 (2011) 19314–19317.

[38] D. Fattakhova-Rohlfing, A. Zaleska, T. Bein, Three-dimensional titanium dioxide nanomaterials, Chem. Rev. 114 (2014) 9487–9558.

[39] Z. Jiang, W. Wei, D. Mao, C. Chen, Y. Shi, X. Lv, J. Xie, Silver-loaded nitrogen-doped yolk-shell mesoporous TiO_2 hollow microspheres with enhanced visible light photocatalytic activity, Nanoscale 7 (2015) 784–797.

[40] W. Li, Z.X. Wu, J.X. Wang, A.A. Elzatahry, D.Y. Zhao, A perspective on mesoporous TiO_2 materials, Chem. Mater. 26 (2014) 287–298.

[41] Z. Jin, F. Wang, J.X. Wang, J.C. Yu, J.F. Wang, Metal nanocrystal-embedded hollow mesoporous TiO_2 and ZrO_2 microspheres prepared with polystyrene nanospheres as carriers and templates, Adv. Funct. Mater. 23 (2013) 2137–2144.

[42] G. Kaune, M. Memesa, R. Meier, M.A. Ruderer, A. Diethert, S.V. Roth, M. D'Acunzi, J.S. Gutmann, P. Müller-Buschbaum, Hierarchically structured titania films prepared by polymer/colloidal templating, ACS Appl. Mater. Interfaces 1 (2009) 2862–2869.

[43] F. Cesano, D. Pellerej, D. Scarano, G. Ricchiardi, A. Zecchina, Radially organized pillars in TiO_2 and in TiO_2/C microspheres: Synthesis, characterization and photocatalytic tests, J. Photochem. Photobiol., A 242 (2012) 51–58.

[44] Y. Ma, G. Ji, B. Ding, J.Y. Lee, Facile solvothermal synthesis of anatase TiO_2 microspheres with adjustable mesoporosity for the reversible storage of lithium ions, J. Mater. Chem. 22 (2012) 24380–24385.

[45] F.H. Schacher, P.A. Rupar, I. Manners, Functional block copolymers: nanostructured materials with emerging applications, Angew. Chem. Int. Ed. 51 (2012) 7898–7921.

[46] D. Chen, S. Park, J.T. Chen, E. Redston, T.P. Russell, A simple route for the preparation of mesoporous nanostructures using block copolymers, ACS Nano 3 (2009) 2827–2833.

[47] Y. Zhang, H. Tan, H. Li, Y.Q. Liu, F.C. Kartawidjaja, Z.C. Yang, J. Wang, Hybrid titania microspheres of novel superstructures templated by block copolymers, Chem. Mater. 23 (2011) 2745–2752.

[48] M.D. Ye, D.J. Zheng, M.Y. Wang, C. Chen, W.M. Liao, C.J. Lin, Z.Q. Lin, Hierarchically structured microspheres for high-efficiency rutile TiO_2-based dye-sensitized solar cells, ACS Appl. Mater. Interfaces 6 (2014) 2900–2908.

[49] M.C. Orilall, U. Wiesner, Block copolymer based composition and morphology control in nanostructured hybrid materials for energy conversion and storage: solar cells, batteries, and fuel cells, Chem. Soc. Rev. 40 (2011) 520–535.

[50] D. Li, Q. Qin, X.C. Duan, J.Q. Yang, W. Guo, W.J. Zheng, General one-pot template-free hydrothermal method to metal oxide hollow spheres and their photocatalytic activities and lithium storage properties, ACS Appl. Mater. Interfaces 5 (2013) 9095–9100.

[51] Y.F. Li, Z.Q. Sun, J.H. Zhang, K. Zhang, Y.F. Wang, Z.H. Wang, X.L. Chen, S.J. Zhu, B. Yang, Polystyrene@TiO_2 core-shell microsphere colloidal crystals and nonspherical macro-porous materials, J. Colloid Interface Sci. 325 (2008) 567–572.

[52] J. Perlich, L. Schulz, M.M. Abu Kashem, Y.J. Cheng, M. Memesa, J.S. Gutmann, S. V. Roth, P. Muller-Buschbaum, Modification of the morphology of P(S-b-EO) templated thin TiO_2 films by swelling with PS homopolymer, Langmuir 23 (2007) 10299–10306.

[53] M. Saito, Y. Nakano, M. Takagi, N. Honda, A. Tasaka, M. Inaba, Improvement of tap density of TiO_2(B) powder as high potential negative electrode for lithium ion batteries, J. Power Sources 244 (2013) 50–55.

[54] N. Sutradhar, A.K. Biswas, S.K. Pahari, B. Ganguly, A.B. Panda, Fluoride free synthesis of anatase TiO_2 nanocrystals with exposed active {001} facets, Chem. Commun. 50 (2014) 11529–11532.

[55] Z. Zhao, Z. Sun, H. Zhao, M. Zheng, P. Du, J. Zhao, H. Fan, Phase control of hierarchically structured mesoporous anatase TiO_2 microspheres covered with {001} facets, J. Mater. Chem. 22 (2012) 21965–21971.

[56] N. Roy, Y. Sohn, D. Pradhan, Synergy of low-energy {101} and high-energy {001} TiO_2 crystal facets for enhanced photocatalysis, ACS Nano 7 (2013) 2532–2540.

[57] L. Yu, X.F. Yang, J. He, Y. He, D.S. Wang, A fluorine free method to synthesize nitrogen and lanthanum co-doped TiO_2 nanocrystals with exposed {001} facets for enhancing visible-light photocatalytic activity, J. Mol. Catal. A – Chem. 399 (2015) 42–47.

[58] J. Lee, Y.S. Jung, S.C. Warren, M. Kamperman, S.M. Oh, F.J. DiSalvo, U. Wiesner, Direct access to mesoporous crystalline TiO_2/carbon composites with large and uniform pores for use as anode materials in lithium ion batteries, Macromol. Chem. Phys. 212 (2011) 383–390.

[59] L. Zhang, M.S. Tse, O.K. Tan, Y.X. Wang, M.D. Han, Facile fabrication and characterization of multi-type carbon-doped TiO_2 for visible light-activated photocatalytic mineralization of gaseous toluene, J. Mater. Chem. A 1 (2013) 4497–4507.

[60] J. Liu, Q. Zhang, J. Yang, H. Ma, M.O. Tade, S. Wang, J. Liu, Facile synthesis of carbon-doped mesoporous anatase TiO_2 for the enhanced visible-light driven photocatalysis, Chem. Commun. 50 (2014) 13971–13974.

[61] S.K. Parayil, H.S. Kibombo, C.M. Wu, R. Peng, J. Baltrusaitis, R.T. Koodali, Enhanced photocatalytic water splitting activity of carbon-modified TiO_2 composite materials synthesized by a green synthetic approach, Int. J. Hydrogen Energy 37 (2012) 8257–8267.

[62] D.E. Gu, Y. Lu, B.C. Yang, Y.D. Hu, Facile preparation of micro-mesoporous carbon-doped TiO_2 photocatalysts with anatase crystalline walls under template-free condition, Chem. Commun. (2008) 2453–2455.

[63] B. Choudhury, S. Bayan, A. Choudhury, P. Chakraborty, Narrowing of band gap and effective charge carrier separation in oxygen deficient TiO_2 nanotubes with improved visible light photocatalytic activity, J. Colloid Interface Sci. 465 (2016) 1–10.

[64] M.W. Shah, Y. Zhu, X. Fan, J. Zhao, Y. Li, S. Asim, C. Wang, Facile synthesis of defective TiO_{2-x} nanocrystals with high surface area and tailoring bandgap for visible-light photocatalysis, Sci. Rep. 5 (2015).

[65] Y. Xiao, X. Wang, Y. Xia, Y. Yao, E. Metwalli, Q. Zhang, R. Liu, B. Qiu, M. Rasool, Z. Liu, J.-Q. Meng, L.-D. Sun, C.-H. Yan, P. Muller-Buschbaum, Y.-J. Cheng, Green facile scalable synthesis of titania/carbon nanocomposites: new use of old dental resins, ACS Appl. Mater. Interfaces 6 (2014) 18461–18468.

[66] Y. Yao, E. Metwalli, M.A. Niedermeier, M. Opel, C. Lin, J. Ning, J. Perlich, S.V. Roth, P. Muller-Buschbaum, Nano- and microstructures of magnetic field-guided maghemite nanoparticles in diblock copolymer films, ACS Appl. Mater. Interfaces 6 (2014) 5244–5254.

[67] X. Wang, J.-Q. Meng, M. Wang, Y. Xiao, R. Liu, Y. Xia, Y. Yao, E. Metwalli, Q. Zhang, B. Qiu, Z. Liu, J. Pan, L.-D. Sun, C.-H. Yan, P. Muller-Buschbaum, Y.-J. Cheng, Facile scalable synthesis of TiO_2/carbon nanohybrids with ultrasmall TiO_2 nanoparticles homogeneously embedded in carbon matrix, ACS Appl. Mater. Interfaces 7 (2015) 24247–24255.

[68] Y.J. Wang, Q.S. Wang, X.Y. Zhan, F.M. Wang, M. Safdar, J. He, Visible light driven type II heterostructures and their enhanced photocatalysis properties: a review, Nanoscale 5 (2013) 8326–8339.

[69] J. Schneider, M. Matsuoka, M. Takeuchi, J. Zhang, Y. Horiuchi, M. Anpo, D.W. Bahnemann, Understanding TiO_2 photocatalysis: Mechanisms and materials, Chem. Rev. 114 (2014) 9919–9986.

[70] G.Z. Zhang, F. Teng, C.H. Zhao, L.L. Chen, P. Zhang, Y.Q. Wang, C.S. Gong, Z.X. Zhang, E.Q. Xie, Enhanced photocatalytic activity of TiO_2/carbon@TiO_2 core-shell nanocomposite prepared by two-step hydrothermal method, Appl. Surf. Sci. 311 (2014) 384–390.

[71] N.D. Abazovic, M.I. Comor, M.D. Dramicanin, D.J. Jovanovic, S.P. Ahrenkiel, J.M. Nedeljkovic, Photoluminescence of anatase and rutile TiO_2 particles, J. Phys. Chem. B 110 (2006) 25366–25370.

[72] S. Mathew, A.K. Prasad, T. Benoy, P.P. Rakesh, M. Hari, T.M. Libish, P. Radhakrishnan, V.P.N. Nampoori, C.P.G. Vallabhan, UV–Visible photoluminescence of TiO_2 nanoparticles prepared by hydrothermal method, J. Fluoresc. 22 (2012) 1563–1569.

[73] J. Jin, S.-Z. Huang, J. Liu, Y. Li, D.-S. Chen, H.-E. Wang, Y. Yu, L.-H. Chen, B.-L. Su, Design of new anode materials based on hierarchical, three dimensional ordered macro-mesoporous TiO_2 for high performance lithium ion batteries, J. Mater. Chem. A 2 (2014) 9699–9708.

[74] T. Lan, Y. Liu, J. Dou, Z. Hong, M. Wei, Hierarchically porous TiO_2 microspheres as a high performance anode for lithium-ion batteries, J. Mater. Chem. A 2 (2014) 1102–1106.

[75] H.B. Wu, J.S. Chen, H.H. Hng, X.W. Lou, Nanostructured metal oxide-based materials as advanced anodes for lithium-ion batteries, Nanoscale 4 (2012) 2526–2542.

[76] J. Wang, Y. Zhou, Y. Hu, R. O'Hayre, Z. Shao, Facile synthesis of nanocrystalline TiO_2 mesoporous microspheres for lithium-ion batteries, J. Phys. Chem. C 115 (2011) 2529–2536.